# UC Berkeley
## UC Berkeley Electronic Theses and Dissertations

**Title**
Structural studies of the microtubule and its regulation

**Permalink**
https://escholarship.org/uc/item/63n82128

**Author**
Eshun-Wilson, Lisa

**Publication Date**
2019

Peer reviewed|Thesis/dissertation

Structural studies of the microtubule and its regulation

By

Lisa Eshun-Wilson


A dissertation submitted in partial satisfaction of the

requirements for the degree of

Doctor of Philosophy

in

Molecular Cell Biology

in the

Graduate Division

of the

University of California, Berkeley


Committee in charge:

Professor Eva Nogales, Chair
Professor James Hurley
Professor Georjana Barnes
Professor Luke Lee

Fall 2019

Structural studies of the microtubule and its regulation

©2019

By

Lisa Eshun-Wilson

# Abstract

Structural studies of the microtubule and its regulation

By Lisa Eshun-Wilson

Doctor of Philosophy in Molecular Cell Biology

University of California, Berkeley

Microtubules (MTs) are highly conserved, cytoskeletal polymers that are involved in a large number of cellular processes. These include cell motility, in which they form the central scaffold of the beating machinery in cilia or flagella, to intracellular transport, in which they function as the cellular highways for the shipment of organelles and other cargos by motor proteins of the kinesin and dynein families, or cell division, in which they form the mitotic spindle to carefully segregate genetic material. These polymers undergo dynamic instability, the stochastic switching between growth and shrinkage, which give them the capacity to rapidly rearrange to allow the cell to grow, move, or divide[1]. Dynamic instability misregulation can cause cancer, Alzheimer's disease, and other life-threatening diseases. Therefore, it is crucial to understand how MTs, and the chemicals or proteins that regulate them, work. For example, the molecular mechanism of α-tubulin acetylation (αK40) has remained elusive, although this chemical modification has been shown to correlate with stability of MTs and serves as a prognostic marker for breast cancer[2,3]. In addition, how MAPs transform large MT substructures is an emerging frontier waiting to be explored.

While it is known that αK40 acetylation is associated with more stable MTs, it is not clear whether the relationship between this chemical modification and stability is causative. To tackle this controversy, I applied a reductionist approach to tease out the direct effects of this modification on MT structure by using cryo-electron microscopy (cryo-EM) to visualize acetylated and deacetylated MTs. I showed that acetylation changes the conformational ensemble of the intraluminal αK40 loop in α-tubulin and may serve as an evolutionarily conserved 'electrostatic switch' to regulate MT stability[4]. Due to the high flexibility of the loop, unlocking the effects of this modification required an exciting hybrid EM-MD approach, designed in collaboration with Dr. James Fraser at UCSF and Dr. Massiliano Bonomi at the University of Cambridge.

As a result of my studies, I have become very interested in conformational heterogeneity and plasticity in the MT lattice. For example, the structure and mechanics of the lattice are not only dependent on the modification state of each tubulin, but also on tubulin isotypes, interacting drugs, or MT-binding partners, all of which can cause changes in tubulin structure and subunit packing within the MT and affect local mechanical strain and other physical properties of the lattice5. I started to appreciate the MT as an allosteric macromolecular machine that interprets multifaceted inputs and reacts by transforming its conformation, stiffness and dynamics[5]. This appreciation launched an exploratory project into the complex world of therapeutic agents,

specifically on lankacidins, a unique class of antibiotics. Similar to PTMs and MAPs, therapeutic agents can affect MT structure and stability. Taxol, a major breast cancer chemotherapy agent, can block the cell cycle in its G1 or M phases by stabilizing MTs and limiting MT critical dynamics[6,7]. Surprisingly, lankacidins (LCs) were shown to have both in vivo antitumor activity in multiple cancer cell lines and antimicrobial activity against Gram-positive pathogens. We observed that LC did not polymerize MTs in a taxol-like manner and now believe that the proposal that its in vivo antitumor activity occurs via MTs could be due to previous lack of proper experimental controls. Thus, we shifted our focus to the effects of LC on bacterial translation and its role as an antibiotic. We present a 2.8 Å structure of the LC-ribosome complex, which improves upon the existing model and shows that LC ring closure is imperative for its mechanism of action. This mechanism may be conserved across related metabolites in the lankacidin class for their antibiotic activity.

## Dedication

To my heart and soul: Sierra and Jeremiah. You give my life purpose.

# Acknowledgements

I would like to extend a special thank you to my family, especially my parents, Vivian and Robert, and my younger siblings, Franceen, Erick, Jazzy, Sierra, and little Jeremiah, for their unwavering support. Their love is why I am who I am today, undoubtedly. I'll never forget when my youngest brother said, "You get paid to think, problem-solve, and travel the world to share solutions – that sounds ideal." He captured my love and enthusiasm for life-long learning in just a few short words. I would also love to thank my lovely girlfriends, Unique, Esmeralda, Stefanie, Nicole, Marta, Lana, Pauline, Joanna, Kirsten, Neeru, Sarah, Lindsey, and, of course, my partner in crime and future co-PI, Michelle for their love and continuous support.

In addition to my amazing family and friends, I would like to thank my mentor Eva Nogales. From the moment I met her, she made me feel special, valued and like I belonged, which is incredibly rare for me. She was my advisor, protector, and my guide through feelings of confusion, isolation or despair. I'll never forget how much time she carved out to help me prepare and crush my qualifying exam. As one of the few African American women to ever pursue structural biology, I felt the weight of the world on my shoulders and extreme pressure to do well to challenge stereotypes and make history. Eva helped me feel prepared, safe, and confident. Patricia, Teresa and Jie, her loyal disciples, made sure to support me daily and locally, which I will be forever grateful for. I am also super grateful to the microtubule team: Rui Zhang, Liz Kellogg, and Ben LaFrance for unforgettable mentorship and major efforts to ensure I understood and mastered the skills I needed to succeed. I would also love to thank my labmates for creating an enriching, collaborative scientific environment that allowed me to thrive as a scientist!

I seem to have struck gold when Jamie Fraser decided to take a sabbatical at UC Berkeley to learn cryo-EM. Eva strategically paired him with me to help me quantitatively show that acetylation transforms the conformation of the αK40 loop while I taught him how to prepare, screen, image and analyze samples for cryo-EM. It was a match made in heaven! I not only gained a brilliant collaborator but also spectacular mentor and friend. In addition to Jamie, Susan Marqusee, Jim Hurley, Georjana Barnes, Luke Lee, Amy Herr, Andy Martin, Ahmet Yildiz, Diana Bautista, David Weisblat and Iswar Hariharan have been beyond supportive. Whether it was a letter of recommendation, a new technique to learn, or grant-writing advice, their support has been invaluable. I am also extremely grateful for all the new places my science and STEM advocacy work took me: Hong Kong, China, Heidelberg, Germany, Paris, France, and even Salvador, Brazil!

And finally, my boys. One benefit of being in a male-dominated field, is it becomes clear very quickly who is an ally and who isn't. I'm so grateful for my lab brother Raoul for our long boba walks where he would listen to me talk about my lab troubles, dating woes, and dream outfits. He is so thoughtful and an amazing listener. And Luke, for not only being an insightful, perceptive scientific collaborator but being a remarkable friend who supported me through failed boyfriends and postdoc interviews. I would also love to thank Dan for introducing me to some of the best burritos Berkeley has to offer, showing me everything I need to know on the Arctica and the

# Table of Contents

**Chapter 3:** Effects of the therapeutic agent Lankacidin C (LC) on MT and ribosome function

3.1 Results and discussion

3.2 Materials and Methods

**Chapter 4:** Conclusions and future directions

# Chapter 1: Introduction to microtubules, their regulatory factors, and cryo-electron microscopy

This chapter will delve into the structure, biogenesis, and mechanics of these essential cytoskeletal polymers as well as the modulators that can tailor their function in the cell. I also discuss the techniques we can use to tease these complex processes apart, specifically cryo-electron microscopy (cryo-EM).

## 1.1 Introduction to microtubules

MTs are highly conserved cytoskeletal polymers that play essential roles in intracellular transport, cell division and cell motility in all eukaryotes. They are assembled from heterodimers of α- and β-tubulin (50kDa each), which stack longitudinally, or head-to-tail, into polar protofilaments (PFs), with ~13 PFs that laterally associate to form a hollow tube[8]. These lateral contacts, which are essential for MT growth, involve the H2-H3 and H1'-S2 loops of one monomer interacting with the M-loop of its neighbor. Lateral contacts are homotypic (α-α and β-β contacts), except at the "seam", where the contacts are now heterotypic (α-β and β-α contacts) and presumably weaker (Fig. 1)[9].
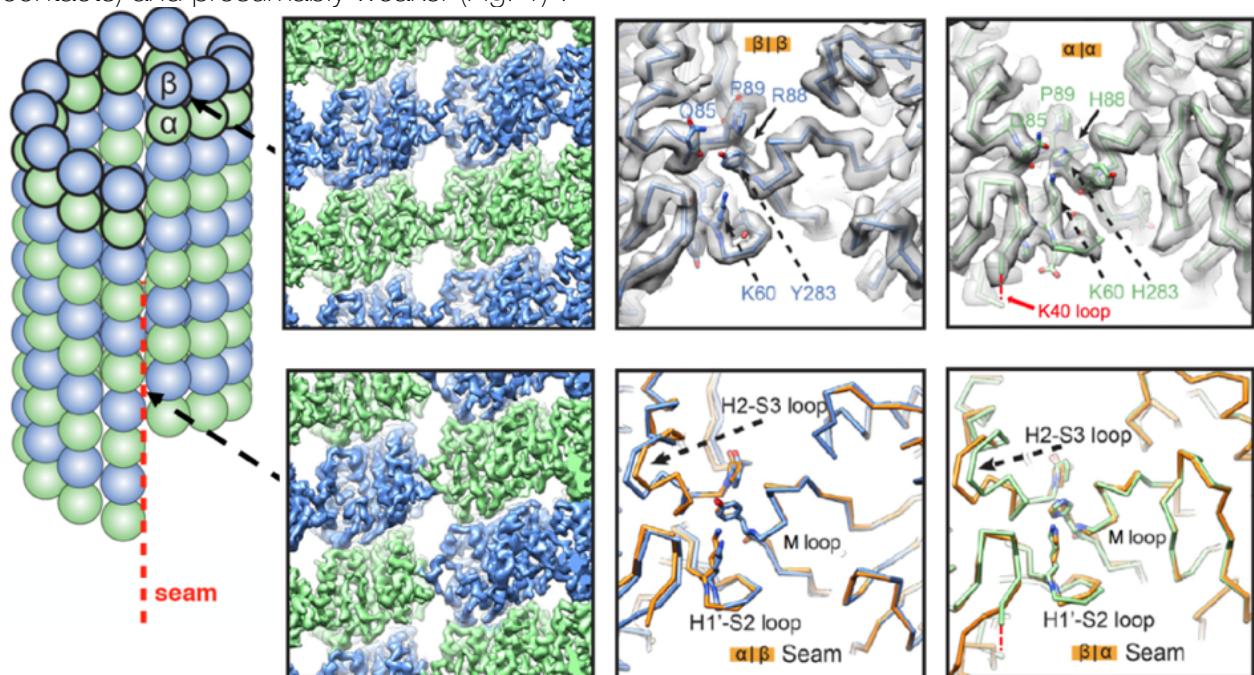


Figure 1 | MT structure and lateral interactions. Schematic of MT structure showing the seam (α-tubulin: green, β-tubulin: blue), to the left. In the top panel, cryo-EM density map at 3.3 Å resolution showing the important residues for homotypic lateral interactions, viewed from the lumen side. The αK40 loop is highlighted in red to emphasize its close proximity to lateral contacts, however, its current structure remains unknown. In the bottom panel, comparisons of the atomic models of the lateral interactions at the seam (orange) and the non-seam (blue for β-β and green for α-α) contacts. Modified from Zhang et al., Cell, 2015 and Nogales and Zhang, Current Opinion in Structural Biology, 2016.

The tubulin arrangement just described gives rise to a polar tube which exposes β-tubulin at the 'plus-end', or the end that preferentially undergoes growth or shrinkage, also known as dynamic instability[10–12]. Powered by guanine triphosphate (GTP) hydrolysis, dynamic instability is defined by: (i) the rate of growth or polymerization, (ii) the rate of shrinkage or depolymerization, (iii) the catastrophe frequency (the rate of switching from a growing to a shrinking state), and (iv) the rate of rescue (the rate of switching from a shrinking to a growing state)[13,14].

Dynamic instability is critical for a plethora of cellular processes, including the coordination of chromosomes segregation and precise assembly of the mitotic spindle during mitosis. Thus, errors in chemical modifications that mark MT stability or mutations in microtubule-associated proteins (MAPs) that modulate MT dynamics could lead to life-threatening diseases. Thus, it is imperative to gain mechanistic insight into how MTs function in order to create potent therapeutic agents to combat MT-related diseases.

### 1.1.1 Microtubule structure and function

Tubulin belongs to a unique class of GTPases, composed of tubulin, which is found in all eukaryotes, and filamenting temperature sensitive strain Z (FtsZ), which is found in eubacteria and archaea. Tubulin and FtsZ share a common fold of two domains, an N-terminal, nucleotide-binding domain with a Rossmann fold that connects by a central or core helix (H7), to a smaller, Intermediate domain, which in b-tubulin includes the taxol bind pocket (Fig. 2). Additionally, tubulin contains a C-terminal domain that includes the H11 and H12 helices that serve as a platform for the binding of many MAPs.

To form αβ-heterodimers, each monomer is folded individually through a heavily regulated two-step folding pathway. First, the nascent α-tubulin and
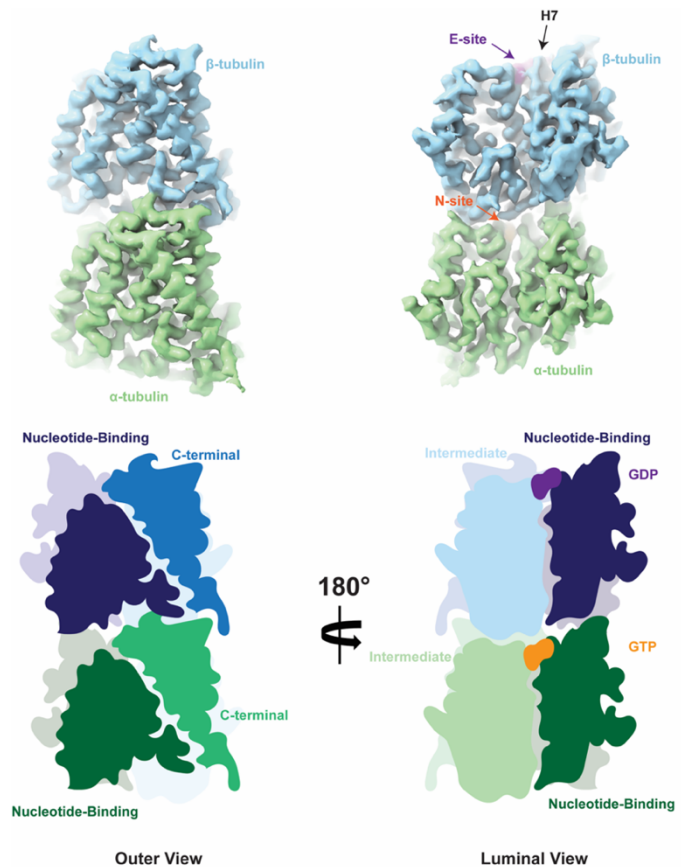


**Figure 2 |** αβ-tubulin heterodimers are the basic building blocks of MT structure. The top panel displays a closeup view of α-tubulin in green and β-tubulin in blue. The non-exchangeable site (N-site) where GTP binds in α-tubulin is highlighted in orange, while the exchangeable site (E-site) where GDP binds in β-tubulin is highlighted in purple. The lower panel shows schematics of each domain within tubulin (Nucleotide-binding domain, navy blue in β and dark green in α; C-terminal domain, royal blue in β and bright green in α; Intermediate or taxol-binding domain, sky blue in β and light green in α) are shown in the panel below. Helix 7 (H7) is the central helix that unites the Nucleotide-binding and Intermediate domains (indicated by black arrow). Each dimer is shown from the outer and luminal views.

β-tubulin chains each associate with prefoldin, which delivers them to the cytosolic chaperonin TRiC (TCP-1 Ring Complex, also called CCT for chaperonin containing TCP-1)[15,16]. Once released from the TRiC, six tubulin folding cofactors (TFC-A, TFC-B, TFC-C, TFC-D, TFC-E and ARL2) bind sequentially to either tubulin subunit and then to both to coordinate subunit synthesis and the formation of the heterodimer[17,18].

In vivo, MTs are largely composed of 13-PFs. It has been proposed that this selection (which is distinct for what is seen in vitro in the absence of microtubule-associated proteins (MAPs), may be due to their nucleation by the γ-tubulin ring complex, which has been proposed to template 13-PF MTs, or by regulation via MAP-binding that promotes 13-PF MTs, as seen for end-binding proteins (EBs) and doublecortin in vitro[19]. Along the MT lattice, PFs stagger giving rise to a pseudo-helical arrangement, where, if we ignore the subtle differences between αβ tubulin heterodimers, the polymer can be seen as a 3-start helix of tubulin monomers. A 3-start, 13-PF MT with homotypic contacts at all lateral interfaces, but the seam, appears to be the most common species found in vivo[19,20].

The process of MT disassembly is driven by GTP hydrolysis. Thanks to α-tubulin's built-in GTPase activity, or ability to hydrolyze GTP, MTs can harvest hydrolysis energy and release it explosively to do work. In tubulin, the catalytic residue E254 resides in loop T7 between H7 and H8 in α-tubulin and hydrolyzes GTP in the exchangeable nucleotide site (E-site) in β-tubulin[9]. Notably, GTP in α-tubulin lies at the intradimer interface in the non-exchangeable site (N-site) and serves as a structural cofactor of tubulin[8,9,21] (Fig. 2). Hydrolysis from GTP to GDP at the E-site causes an important conformational change, or a lattice compaction (REFs), which generates strain that breaks lateral contacts. Specifically, the lattice compaction describes a decrease in the dimer rise, or "axial repeat", which is the distance between dimers along a protofilament.

The nucleotide-binding domain is exceptionally rich in aromatic residues, making it highly resilient. It consists of a parallel β-sheet (S1-S6) and α-helices H0-H7 (Fig. 3A), each of which are connected by loops T1-T6[10] (Fig. 3B). Each of six loops attach one β-strand to a neighboring α-helix and play an important role in stabilizing with the nucleotide. The intermediate domain consists of α-helices H8-10 and a mixed β-sheet (S7-S10) and the C-terminal domain completes the structure with two antiparallel β-strands S11-S12 and two highly negatively charged helices H11-H12. The terminal residues of H12 (~10 residues for α and ~20 for β) also known as the C-terminal tails, are highly charged, flexible and acidic and serve as a major interaction site for PTMs and MAPs[9,10,22] (Fig. 3).
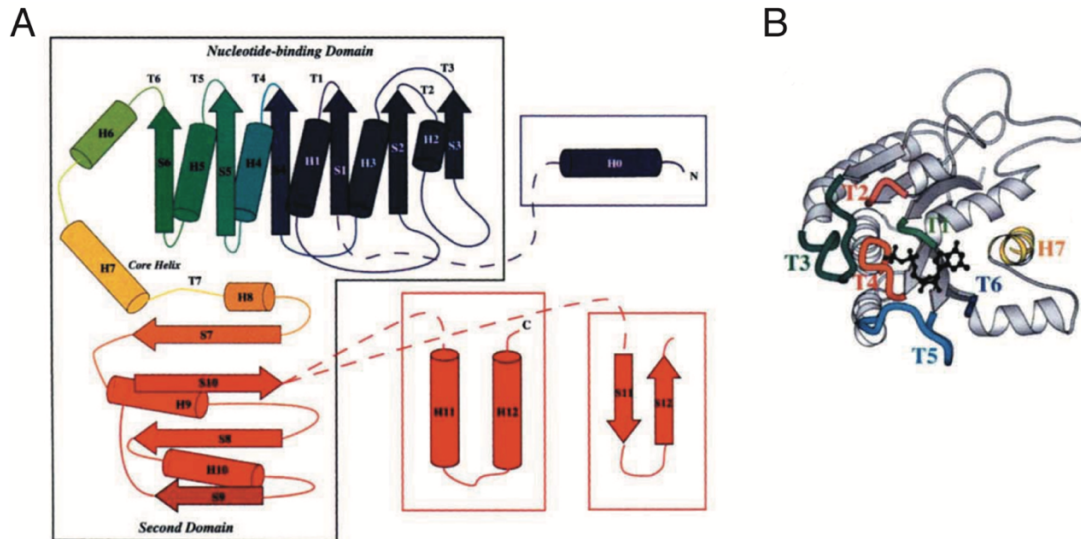
**Figure 3** | Outline of the structural domains and nucleotide binding site of tubulin. (A) Secondary structure β-strands and α-helices are numbered H0-H12 and S1-S12 and mapped to their corresponding structural domains (nucleotide binding domain (α-helices H0-H7 and β-strands S1-S6); Intermediate domain (α-helices H8-10 and β-strands S7-S10); C-terminal domain (α-helices H11-H12 and β-strands S11-S12). (B) Top-view of β-tubulin monomer highlighting GDP bound to the E-site and interacting with loops T1-T6. Adopted from Nogales et al. Nature, 1998.

To form αβ-heterodimers, each monomer is folded individually through a heavily regulated two-step folding pathway. First, the nascent αβ-tubulin chains associate with the chaperone protein prefoldin, which delivers them to the cytosolic chaperonin TRiC (TCP-1 Ring Complex, also called CCT for chaperonin containing TCP-1)[15,16]. Once released from the TRiC, six tubulin folding cofactors (TFC-A, TFC-B, TFC-C, TFC-D, TFC-E and ARL2) bind either αβ-tubulin subunit and coordinate subunit synthesis and the formation of the heterodimer[17,18]. This process interweaves the β-sheets and α-helices to form the domain architecture that empower tubulin to perform its unique GTPase enzymatic activity.

In tubulin, the catalytic residue E254 for GTP hydrolysis resides in loop T7 between H7 and H8 in α-tubulin and hydrolyzes GTP in the exchangeable nucleotide site (E-site) in β-tubulin[9]. Notably, GTP in α-tubulin lies at the intradimer interface in the non-exchangeable site (N-site) and serves as a structural cofactor of tubulin[8,9,21] (Fig. 2). Hydrolysis from GTP to GDP-$P_i$ at the E-site causes a global conformational change, or a lattice compaction, which generates strain that breaks lateral contacts. Specifically, the lattice compaction describes a decrease in the dimer rise, or "axial repeat", which is the distance between dimers along a protofilament.

Lattice compaction and strain generation events lead to the following changes along longitudinal contacts at the E-site in β-tubulin: local rearrangements within α:T7-H8, β:T2-H2, and β:T5, the release of the coordinating $Mg^{2+}$ ion, and a shift in the position of α:E254 for catalysis[9]. These changes promote the release of phosphate and result in the final GDP state in the body of the MT. More specifically, there is a distortion in the α:H8 post-hydrolysis (GDP-

like) state and not the pre-hydrolysis (GTP-like) state. The distortion in α:H8 is suspected to generate strain in the lattice, suggesting that GTP hydrolysis provokes a global, longitudinal strain that builds up gradually in addition to lateral strain propagation, until a threshold is reached, leading to an abrupt release of the excess strain. A second conformational change in the GDP-like state that may also contribute to mechanical strain is the rotation of the intermediate domain and C-terminal helices (H11-H12) of α-tubulin relative to its N-terminal domain. As the heterodimer rotates, it moves further away from its proposed ground state, based on previously published crystal structures. The build-up of mechanical strain in the GDP-like state can lead to explosive release of energy that is hypothesized to pop the "GTP-stabilizing cap". A growing MT contains a stabilizing GTP-cap (or an accumulation of tubulin dimers with GTP at the E-site). This 'cap' disappears when GTP hydrolysis or Pᵢ release happens faster than the addition of new dimers, for example, at concentrations of tubulin lower than its critical concentration or in the presence of depolymerizing MAPs, leading to MT catastrophe[1].

The role that the seam plays in MT catastrophe remains unknown. Some support the seam-centric model, which asserts that the build-up of longitudinal tension and mechanical strain leading to GTP hydrolysis destabilizes MTs starting at the seam interface[23]. Whereas, others support a more holistic model, which argues that the seam plays a passive role in MT instability and MT catastrophe is caused by the weakening of lateral contacts (first between α-α subunits followed those between β-β subunits) paired with the strengthening of longitudinal contacts, but without the influence of mechanical strain build-up within the lattice[23].

### 1.1.2  Introduction to the MT chemical modification: αK40 tubulin acetylation

Dynamic instability is highly regulated in vivo by multiple mechanisms that affect tubulin and its interaction with a myriad of regulatory factors. One mechanism that cells can use to manipulate MT structure and function involves the posttranslational modification (PTM) of tubulin subunits. Through the spatial–temporal regulation of proteins by the covalent attachment of additional chemical groups, PTMs can play important roles in controlling the stability and function of MTs[24]. Most of tubulin PTMs alter residues within the highly flexible and negatively charged C-terminal tail of tubulin that extends from the surface of the MT and contributes to the binding of microtubule-associated proteins (MAPs)[25,26]. These PTMs include detyrosination, Δ2-tubulin generation, polyglutamylation, and polyglycylation[27]. However, acetylation of α-tubulin on K40 stands out as the main tubulin PTM that localizes to the inside of the MT, within a loop of residues P37 to D47, often referred to as the αK40 loop. This modification is carried out by α-tubulin acetyltransferase αTAT1 and removed by the NAD⁺-dependent deacetylase SIRT2 and by HDAC6[25,27]. Despite some interesting functional studies concerning this modification, structural insights into the effect of this "hidden PTM" on MT properties are still missing.

Shortly after its discovery over 30 years ago[28], acetylation of αK40 was found to mark stable, long-lived ($t_{1/2} > 2$ h) MT subpopulations, including the axonemes of cilia and flagella or the marginal bands of platelets[25,27], and to protect MTs from mild treatments with depolymerizing drugs, such as colchicine[29] and nocodazole[30]. Multiple studies have suggested that reduced levels of αK40 acetylation cause axonal transport defects associated with Huntington's disease,

Charcot–Marie–Tooth disease, amyotrophic lateral sclerosis, and Parkinson's disease[31–34]. These defects can be reversed by restoring αK40 acetylation levels[35]. On the other hand, elevated levels of αK40 acetylation promote cell–cell aggregation, migration, and tumor reattachment in multiple aggressive, metastatic breast cancer cell lines[36,37]. While these studies imply that tubulin acetylation has an effect on axonal growth and transport, a mechanistic model is still missing.

Whether acetylated MTs are stable because they are acetylated or whether stable structures are better at acquiring this modification remains a point of contention. For example, a previous study showed that acetylation did not affect tubulin polymerization kinetics in vitro[38]. However, this study was confounded by two factors: (i) MTs acetylated by flagellar extract were compared with native brain tubulin, which is ~30% acetylated, and (ii) only a single round of polymerization/depolymerization was performed after in vitro acetylation, which is insufficient to remove αTAT1 or other MAPs. Thus, the results of that study may be limited by the purity and preparation of the sample.

Our previous structural work also found no significant differences between 30% acetylated and 90% deacetylated MTs at a resolution of ~9 Å, particularly at the modification site. The αK40 residue within the αK40 loop, which was invisible in both cases due to the intrinsic disorder and/or to the remaining heterogeneity of the loop (i.e., that study may have been limited by the low purity of the samples)[27]. More recent in vitro studies, using pure samples of 96% acetylated and 99% deacetylated MTs, argue that αK40 acetylation induces a structural change that improves the flexibility and resilience of MTs[39,40]. These studies find that acetylated MTs maintain their flexural rigidity, or persistence length, after repeated rounds of mechanical stress, while deacetylated MTs show a 50% decrease in rigidity and are 26% more likely to suffer from complete breakage events[39,40].

Since the αK40 residue is less than 15 Å away from the lateral interface between PFs, a possible model for the molecular mechanism of acetylation is that it alters inter-PF interactions by promoting a conformation of the αK40 loop that confers flexural rigidity, thus increasing its resistance to mechanical stress—a phenomenon called PF sliding as illustrated in Fig. 4[39,40]. Molecular dynamics (MD) simulations have suggested a model where αK40 forms a stabilizing salt bridge with αE55 within the core of the α-tubulin monomer that in turn stabilizes αH283 within the M-loop of its neighboring α-tubulin monomer[41]. Another study proposed that αK40 acetylation may specify 15-PF MTs, which are known to be 35% stiffer than 13-PF MTs and more effective at forming MT bundles[42].

Given the uncertainties remaining concerning the effect of αK40 acetylation on MTs, we decided to characterize the conformational properties of the αK40 loop in the acetylated and deacetylated MTs that could have an effect on MT structure and properties. To that end, we produced near atomic-resolution cryo-EM maps of 96% acetylated (Ac[96]) and 99% deacetylated (Ac[0]) MTs. By improving sample purity, we were able to visualize more density for the αK40 loop in the acetylated state. Using MD methods to fit the cryo-EM map, we found that acetylation shifts the conformational landscape of the αK40 loop by restricting the range of

motion of the loop. In contrast, in the $Ac^0$ state, the $\alpha$K40 loop extends deeper into the lumen of the MT, and samples a greater number of conformations. These motions are likely to increase the accessibility of the loop to $\alpha$TAT1, in agreement with the hypothesis that $\alpha$TAT1 acts by accessing the MT lumen[43,44], and likely influence lateral contacts, in agreement with the causative effect of acetylation on the mechanical properties of MTs[39]. For more details, please visit Chapter 2.
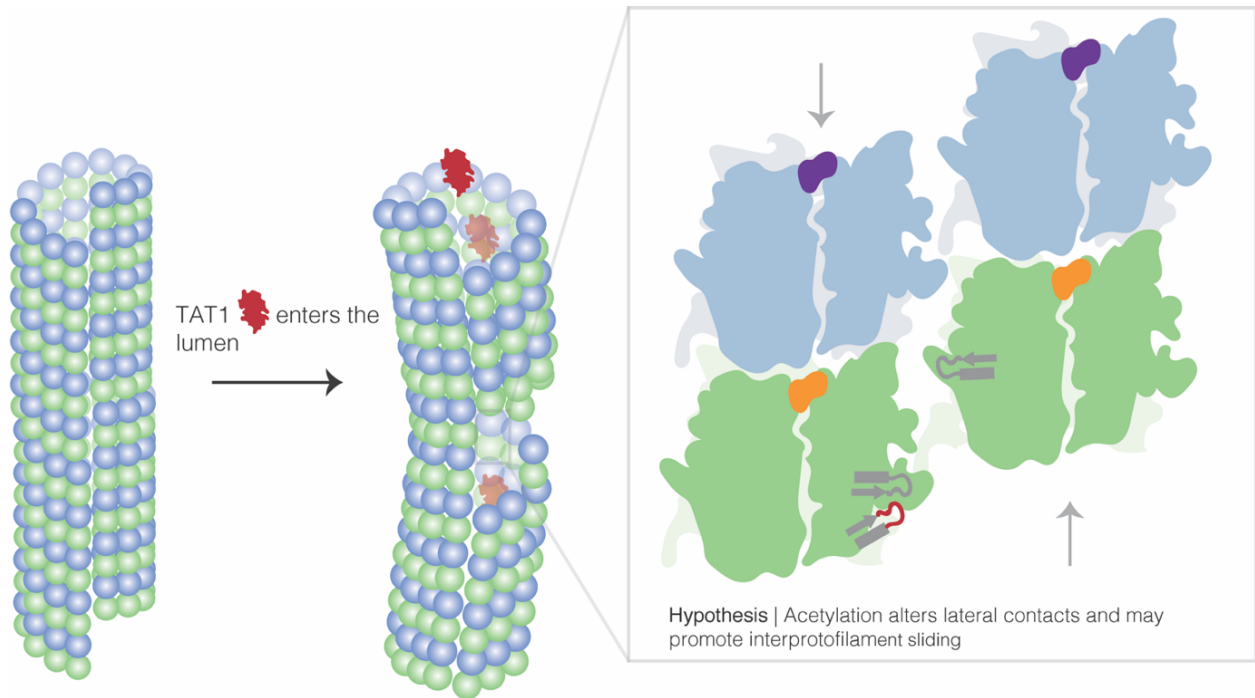


Figure 4 | Hypothesis | Acetylation stabilize MTs by changing lateral contacts and promoting inter-protofilament sliding.

## 1.2: Introduction to cryo-electron microscopy (cryo-EM) and molecular dynamics

### 1.2.1 Cryo-EM in the study of MTs

Cryo-electron microscopy (cryo-EM) is a type of electron microscopy in which the specimen is prepared and imaged at cryogenic temperatures, more specifically, at the boiling point of nitrogen: -196°C. Winner of the 2017 Nobel Prize in Chemistry and the 2015 Method of the Year Winner by Nature Magazine, this technique is superb for imaging biological macromolecules in their native, hydrated state. Joachim Frank, Jacques Dubochet and Richard Henderson, winners of the 2017 Nobel Prize in Chemistry for Cryo-EM, worked tirelessly over several decades to advance this, now, cutting-edge technique. Indisputably, one of its paramount advantages is its ability to analyze large, dynamic macromolecular assemblies. Complex, flexible proteins are too large to analyze by other structural techniques, such as X-ray crystallography, or too heterogenous for ensemble modeling techniques like nuclear magnetic resonance (NMR) spectroscopy, for instance. However, large dynamic complexes or variable, flexible regions within more rigid, globular structures often responsible for some the cells most critical activities, such as the hallmark Alzheimer's marker tau which stabilizes neuronal MTs.

To prepare samples for cryo-EM, proteins are plunge-frozen in liquid ethane on a thin, carbon-coated support layer placed on a copper mesh grid (Fig. 5). This near-instantaneous vitrification and subsequent manipulation in liquid nitrogen allows us to not only capture high resolution structural details but also possible intermediate states of our protein of interest. Cryo-EM has played a pivotal role in elucidating the structure-function relationship of MTs and their PTMs and MAPs. Beginning in the 1990s, researchers began to provide a mechanistic picture
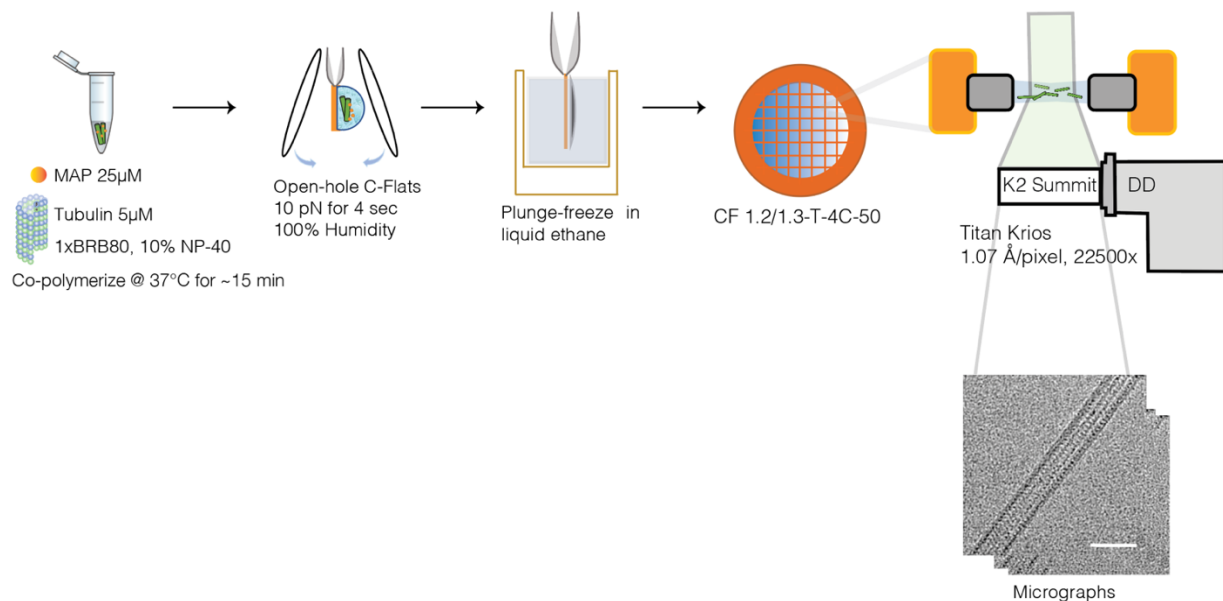


**Figure 5** | Schematic of cryo-EM sample preparation. Proteins are plunge-frozen at cryogenic temperatures on supportive copper grids and imaged using an electron microscope on a direct detector. MAPs are shown in orange and MTs are shown in green.

of how dynamic instability works by using cryo-EM to construct a 3D model of a fully assembled MT polymer at 20 Å[8]. This map showed that the negatively charged C-terminal tails extended from the outer protofilament crest of the MT and served as a major landing and interaction site for a plethora of MAPs. Gaining a deeper mechanistic understanding of MT function and stability immediately became a challenge, however, because of the presence of the seam, which breaks helical symmetry, and the structural similarity between α- and β-tubulin, making it computationally challenging to extract high resolution information at the time.

Thanks to the improvement in data quality and image analysis, our group published MTs in different stages of dynamic instability at 4.7-5.5 Å resolution. The work employed two strategies: to build upon image processing techniques developed by Edward Engelman, Charles Sindelar and Ken Downing to better account for the heterogeneity along the MT lattice; and the motor domain of kinesin as a fiducial marker to differentiate between α- and β-tubulin heterodimers. By comparing the structural transitions at each stage of dynamic instability, our group found that GTP hydrolysis, which powers this fundamental process, leads to a compaction at the exchangeable nucleotide site (E-site) of β-tubulin at the longitudinal inter-dimer interface[9,45]. Soon after, our group went on to visualize not only the different stages of dynamic instability at higher resolution (3.5 Å), but also characterize their regulation by the MAP end-binding 3 (EB3)[9]. Our group showed that EB3 stabilizes a compacted structural intermediate state proposed to correspond to GDP-P$_i$, and that it promotes GTP hydrolysis, thus uncovering the molecular basis for its modulation of MT dynamics. With each new development in the field of cryo-EM, the MT field has propelled further and further, allowing us to now ask more challenging questions. How do tubulin isotypes and their PTMs drive the tubulin code, or, in other words, how cells read and write unique MT populations? How should we define a bona fide MAP? Do MAPs have different or redundant functions and what about their structures dictate that? How are local concentrations and the relative abundance of different MAPs regulated in the cell? What are the implications of misregulated PTMs and MAPs in disease? What role do small molecules play in MT stability?

## 1.2.2 MT image processing and helical processing

As previously mentioned in 1.3.1, our general MT 3D reconstruction approach builds upon the Iterative Helical Real Space Reconstruction (IHRSR) algorithm, featuring new additions for MTs[46,47]. First, as shown in Fig. 6, MT segments are manually selected from motion-corrected micrographs, which can be done using either the APPION image processing suite or the RELION software package[48,49]. Next, individual MT particles are extracted from these segments by dividing the segments into overlapping boxes (512 × 512 pixels) that overlap every 82 Å, which corresponds to an expanded tubulin dimer repeat. Thus, the non-overlapping region captures ~13 unique tubulin dimers with each dimer corresponding to a single asymmetric unit. The raw particle stacks are then compared to 3D MT reference models that range in PF number (11-16). This multi-reference alignment (MSA) protocol can be carried out using the EMAN1 software or using the 3D classification module in RELION[50,51].

Now, in order to orient a raw MT particle image with respect to the 3D reference model, the following five alignment parameters are needed: x, y translations (shx, shy) and three Euler angles ($\Psi$, $\theta$, $\phi$). For a helical object, $\Psi$ is the in-plane rotation, $\theta$ is the out-of-plane tilt, and $\phi$ is the azimuthal angle around the MT axis. With this information, MT particles with the same PF are grouped together and further refined using the FREALIGN software package[52,53].
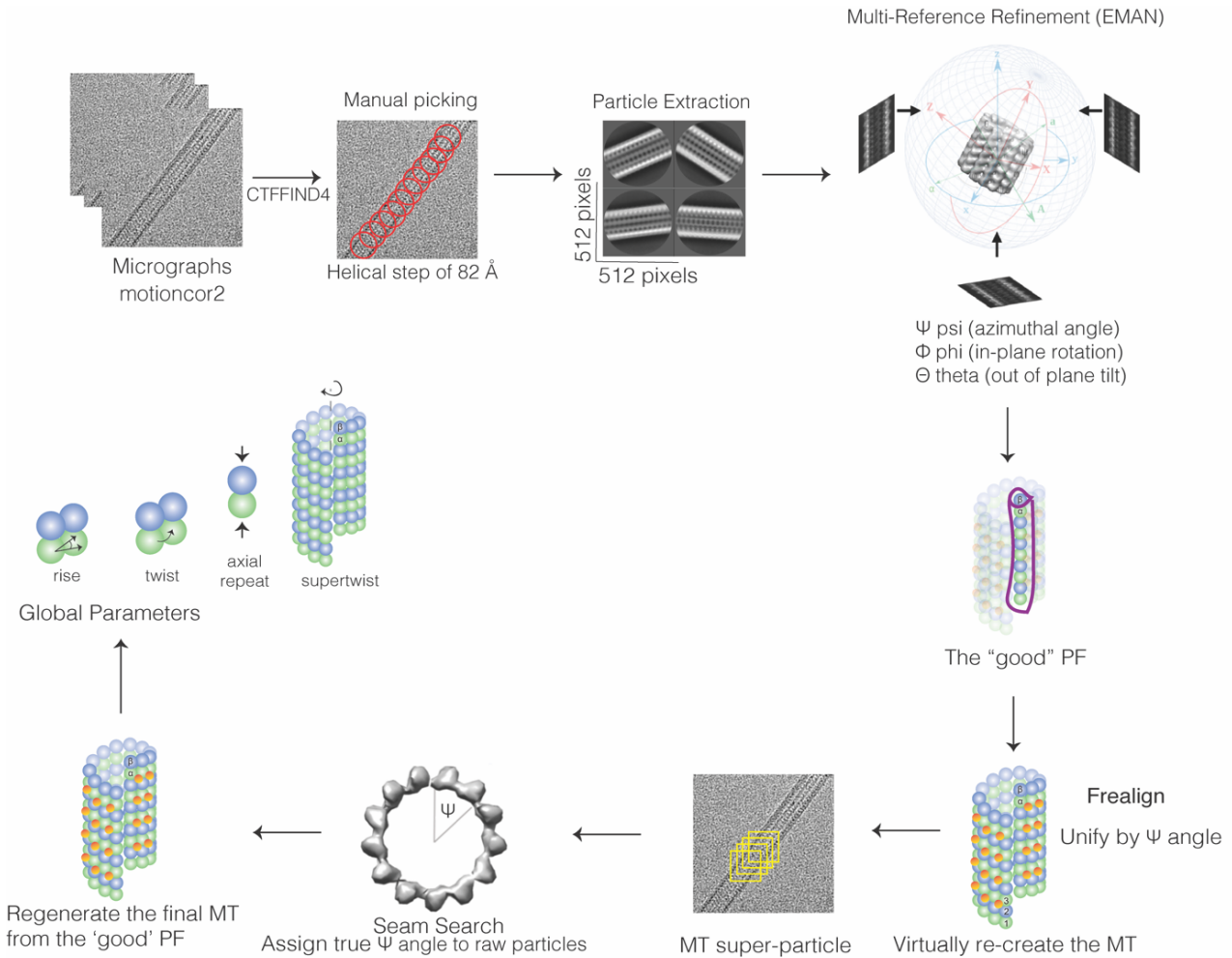


**Figure 6** | Schematic of helical processing pipeline. MT particles are extracted from drift-corrected images and used to generate a 3D model. Using the given helical alignment parameters and the seam location, high resolution 3D MT reconstructions can be generated with high confidence.

There are two types of 3D reconstructions you can generate with FREALIGN: (1) one with pseudo-helical symmetry in which each raw particle is used ~13 times during the reconstruction step (symmetrized) or one without symmetry in which each raw is used only once (C1). In addition, the seam location serves as an important alignment parameter and can be used to generate a high resolution MT model, as previously described[54]. From this model, we can quantify any changes in the global parameters. For example, MAP binding could transform the MT lattice, leaving it more compacted or twisted. Specifically, the global parameters we measure are the rise, or the translation along the helical axis, parallel to the

seam, the twist, or the rotation around the helical axis, the *dimer rise*, or "axial repeat", which is the distance between dimers along a PF, and the *dimer twist* or 'MT supertwist', which describes the angle between protofilaments and the axis of the MT (0 supertwist indicates that the PFs run parallel to the MT axis). These global parameters are also used to further enhance MT particle alignment during iterative refinement tactics and, thus, improve the signal-to-noise ratio in our final reconstruction.

### 1.2.3 Meta-inference molecular dynamics as a complementary tool to EM

Modeling a dynamic, complex system is a challenging task. In cryo-EM you often capture multiple intermediate, highly populated states that are only pieces of the full story. Joachim Frank very beautifully illustrates this point using the reaction of the post-termination ribosome splitting into its subunits, which is catalyzed recycling factor RRF and elongation factor EF-G ● GTP bind to post-termination ribosome[55]. As this reaction proceeds, there is a short-lived intermediate state in which both RRF and EF-G ● GDP are bound to the ribosome, but splitting has not yet occurred. According to kinetic simulations, this state lasts less than 200 ms, and would, thus, be challenging to capture given the slow method of cryo-EM grid preparation described in 1.3.1[55]. And if captured, it would occupy a low number of sub-states that could be averaged out using the conventional image processing pipeline, also described in 1.3.1.

This can be a major issue when studying flexible proteins, flexible regions within proteins and/or proteins sensitive to external factors, such as pH or temperature, because their function is dependent on their ability to interconvert between multiple functional states with ease, including less
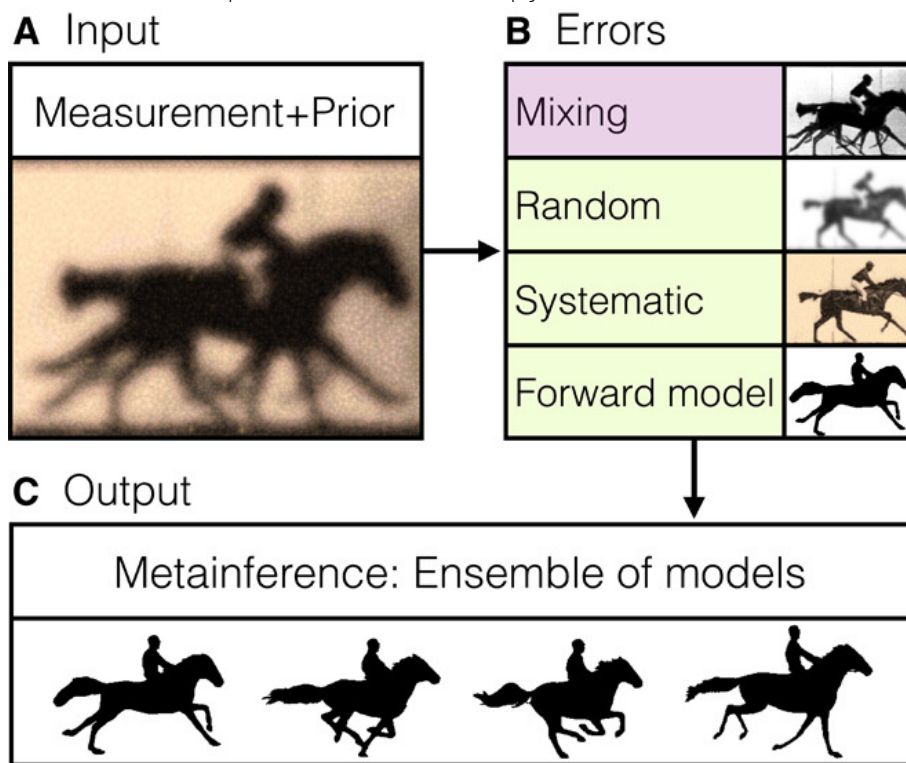


Figure 7 | To generate precise and accurate models from (A) input experimental data, it is imperative to deconvolute the following errors (B): mixing, random, systematic, and forward models, or inherent model bias to successfully extract out a representative ensemble of models (C). This is imperative for dynamic, heterogeneous systems, in which the experimental data is based on a population of states and fluctuations between states. To accomplish this, Bonomi et al. use metainference MD to model a finite sample of this distribution, shown in C, using replica-averaged modeling based on the maximum entropy principle. Adopted from Bonomi et al., Science Advances 2019.

popular sub-states. To address the issue of visualizing a complex system populated by an ensemble of different sub-states, but represented as an average, Drs. Massimiliano Bonomi and Michele Vendruscolo developed an impressive Bayesian inference Molecular Dynamics (MD) method, called "metainference" MD that can identify errors in experimental measurements, such as the mixing of sub-states and random or systematic errors, and deconvolute multiple sub-states from experimental measurements averaged over multiple states[56] (Fig. 7). Metainference MD models a finite sample of the distribution of models using a replica approach, based on the maximum entropy principle[57] and can serve as a complementary tool for cryo-EM, especially when studying flexible proteins and flexible regions within proteins.

Chapter 2: Effects of αK40 tubulin acetylation on MT structure and stability

## 2.1 Results and discussion

This chapter highlights our high resolution cryo-EM structures of human acetylated and deacetylated MT samples, the MD models of the αK40 loop configurations in each state, and the mechanistic insights gained through their interpretation. These results have been published and are discussed in more detail in our recent paper[4].

### 2.1.1 High-resolution cryo-EM reconstructions of pure acetylated (Ac$^{96}$) and deacetylated (Ac$^0$) MTs

Using recent biochemical schemes designed to enrich for specific acetylation states, we generated Ac$^{96}$ and Ac$^0$ MTs for use in our cryo-EM studies[39]. We prepared cryo-EM samples as previously described of Ac$^{96}$ and Ac$^0$ MTs in the presence of end-binding protein 3 (EB3)[45]. EB3 served as a fiducial marker of the dimer that facilitated alignment of MT segments during image processing. Using the symmetrized MT reconstruction, which takes advantage of the
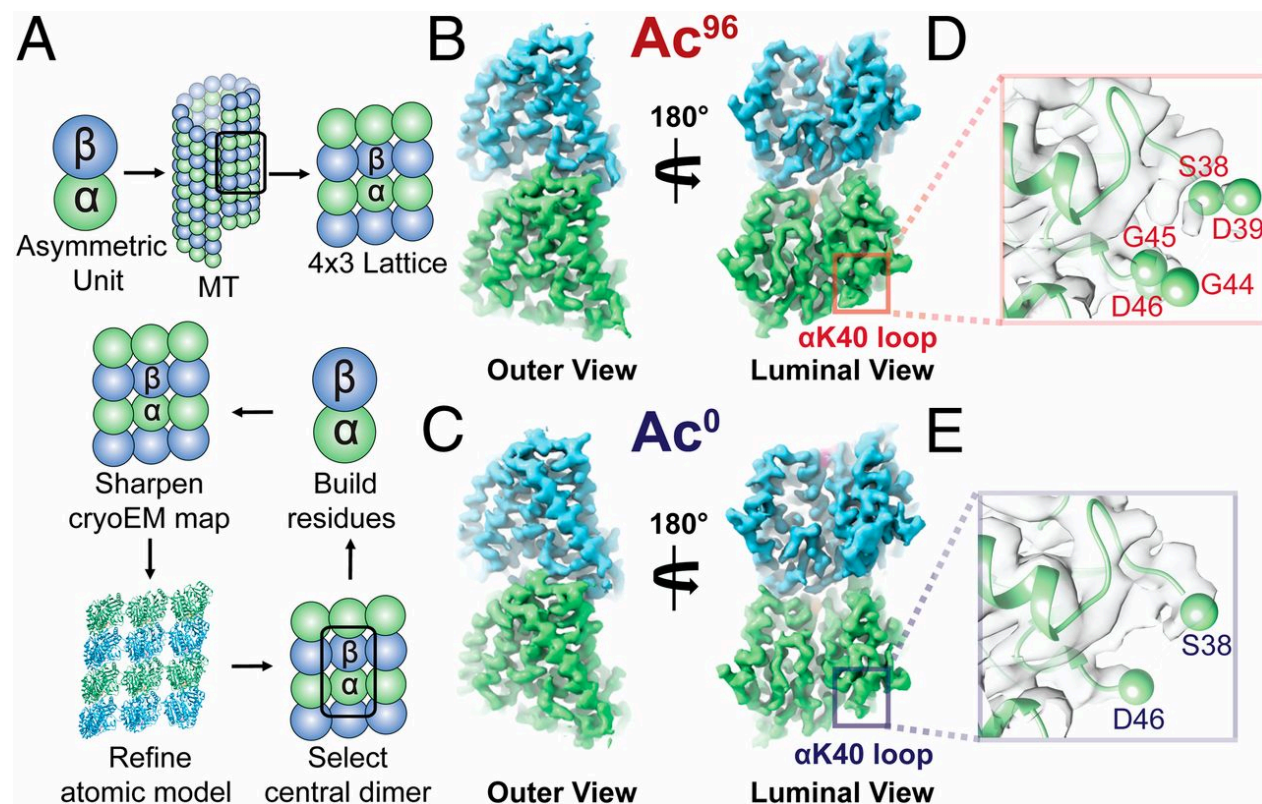


**Figure 8 |** High-resolution maps of 96% acetylated (Ac96) and <1% acetylated (Ac0) MTs. (A) Schematic of the model-building and refinement process in PHENIX. We sharpened a representative 4 × 3 lattice, refined the corresponding atomic structure (3JAR) into our map, and extracted out the cen- tral dimer to build additional residues into the αK40 loop. We performed this process iteratively for both the Ac96 and Ac0. The structure of the Ac96 (B) and Ac0 (C) αβ-tubulin heterodimers, respectively, are shown from the outer and luminal views with close-ups of αK40 loop in each state (D and E) low- pass filtered to 3.7 Å.

pseudo-helical symmetry present in the MT, we extracted a 4 × 3 array of dimers for further B-factor sharpening, refinement, and model building (Fig. 8). This array includes all possible lateral and longitudinal nonseam contacts for the central dimer, which was later extracted for model building and map analysis.

The αK40 loop has been poorly resolved in previous EM reconstructions, and existing models contain a gap between residues Pro37 and Asp48[43]. While the loop has been resolved in a number of X-ray crystallographic structures, the conformations stabilized in the crystal lattice are likely consequences of the presence of calcium and/or crystal contacts (See Fig. S3B in Eshun-Wilson et al. PNAS, 2019 for more details). For our symmetrized maps, we were able to build residues S38–D39 and G44–D47 into the $Ac^{96}$ state and S38 and D46–D47 into the $Ac^0$ state (Fig. 8D and E). Qualitatively, the maps suggest that the αK40 loop is slightly more ordered in the $Ac^{96}$ state, with the protrusion of density following Pro37 extending away from or toward Asp48 in the $Ac^{96}$ or $Ac^0$ states, respectively. However, it is likely that multiple conformations of the loop, perhaps as a function of each loop's individual position around a helical turn, are averaged together and result in the low signal-to-noise levels we observe in the map.

## 2.1.2 Conformational differences across MT states are confirmed by non-symmetrized reconstructions

We considered the possibility that the symmetrizing procedure used to improve signal and resolution in our image analysis was averaging different αK40 loop conformation within different PFs and thus interfering with our interpretation of the loop structure in the two states. To test the hypothesis, we analyzed the nonsymmetrized maps calculated with C1 symmetry for the $Ac^{96}$ and $Ac^0$ states. We extracted a full turn of 13 adjacent dimers. This full-turn map revealed additional density extending out further along the loop in the $Ac^{96}$ state compared with the symmetrized maps filtered to the same resolution (4 Å) (Fig. 9).

Furthermore, the density for the loop observed at the seam was distinct from that at the nonseam contacts. To maximize the interpretability of the subunits making nonseam contacts, we used noncrystallographic symmetry (NCS) averaging as an alternative method to increase the signal-to-noise levels in the maps.

This procedure improved the density for nonglycine backbone atoms in the αK40 loop in the $Ac^{96}$ state, allowing us to trace an initial Cα backbone for this region, while in the $Ac^0$ state the loop remained unmodelable (Fig. 9C and D). This interpretation agrees with the qualitative difference in the density, which indicate less disorder for the $Ac^{96}$ state than $Ac^0$ state, of the traditionally symmetrized and C1 maps.



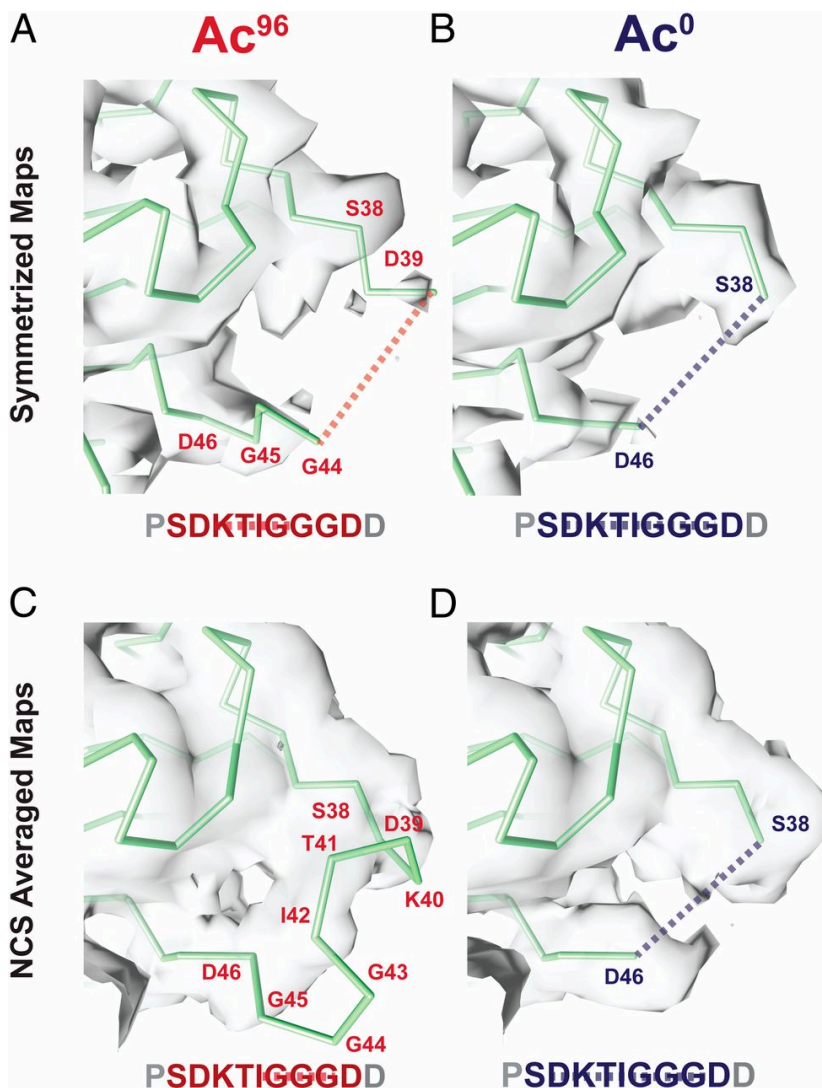**Figure 9** | Symmetrized and NCS-averaged C1 maps of $Ac^{96}$ and $Ac^0$ MTs reveal the αK40 loop is more ordered in the $Ac^{96}$ state. Close-up views of the αK40 loop (P37–D47) in the (A) $Ac^{96}$ and (B) $Ac^0$ states in the symmetrized maps low-pass filtered to 4 Å and the (C) $Ac^{96}$ and (D) $Ac^0$ states in the NCS-averaged C1 maps low-pass filtered to 4 Å. The dotted lines indicate missing residues.

This NCS averaging method had multiple advantages over the traditional averaging technique for pseudohelical processing implemented in FREALIGN. First, the model coordinates used for the averaging are based on the matrix of α-tubulin monomers along a full turn rather than the single α-tubulin monomer. Second, in the FREALIGN averaging approach, the signal from the dimers at the seam are down-weighted, whereas NCS averaging allows us to separate the signal from the seam, and thus to deconvolute the signal from the nonseam locations. Third, this procedure also acts to low-pass filter the map to 4 Å (the high-resolution limit of the C1 map), which should suppress noise from the more disordered parts of the map, including alternative conformations of the αK40 loop. Using this NCS-based approach, we were able to resolve density and build a model for three additional residues, the acetylated K40, T41, and I42. These residues pack toward the globular domain of α-tubulin, consistent with the favorability of burying these relatively hydrophobic residues in the $Ac^{96}$ state. Despite observing only very weak density, we have modeled the glycine-rich region that extends into the lumen as a tight turn, which we note is only possible due to the expanded Ramachandran space accessible to glycine residues (Fig. 9C). In contrast, and despite better global resolution, we did not observe any density consistent with a stable conformation of the loop in the $Ac^0$ map. Based on this result, which is consistent across the NCS-averaged and traditionally symmetrized maps, we did not build any additional residues into the $Ac^0$ density (Fig. 9D).

### 2.1.3 Ensemble modeling of the αK40 loop in each state using density-restrained MD

For regions that exhibit a high degree of disorder, like the αK40 loop, a single, static structure is a poor description of the native state. Ensemble models can help to elucidate how populations of conformations change upon perturbations, such as PTMs[58,59]. To derive an ensemble of conformations representing the $Ac^{96}$ and $Ac^0$ states, we used the atomic structure built into the $Ac^{96}$ map as the starting model to initiate metainference-based MD simulations, which augment a standard force field with a term representing the density derived from the cryo-EM map[60]. In contrast to molecular dynamics and flexible fitting (MDFF) and other refinement methods that seek to converge on a single structure[61], this method models a structural ensemble by maximizing the collective agreement between simulated and experimental maps, and accounts for noise using a Bayesian approach[62]. Initiating simulations for both the $Ac^{96}$ and $Ac^0$ states from starting models that differ only in the acetyl group and distinct input experimental density maps allowed us to test whether acetylation restricts the motion of the loop, trapping it in a tighter ensemble of conformations.

To analyze the conformational dynamics of the loop, we analyzed the root-mean-square fluctuations of residues 36–48 within replicas for each simulation. This analysis shows that the αK40 loop fluctuations are more restricted in the $Ac^{96}$ state than in the $Ac^0$ state (Fig. 10A). Next, we analyzed the distribution of conformations adopted by the loop by analyzing the distance between K40 and the globular domain of α-tubulin (represented by L26) and by clustering together the snapshots from all replicas of both simulations based on the root-mean-square deviations (RMSDs) of residues 36–48. Similar to the starting reference model, where the distance is 10.6 Å, $Ac^{96}$ is enriched in conformations that pack close to the globular domain of the α-tubulin core (Fig. 10B). These conformations, exemplified by clusters 1, 4, and 6,

position the acetylated K40 to interact with residues along H1. In contrast, the $Ac^0$ state favors conformations that extend toward the MT lumen, as exemplified by clusters 0, 2, 5, 7, and 8 (Fig. 10B). Clusters 3, 9, 10, and 11, labeled in gray, had equal numbers of frames enriched in $Ac^{96}$ and $Ac^0$ and sampled rare (<5%) extreme states on both the exposed and packed ends of the conformational spectrum (Fig. 10B).

These computational results are consistent with the visual analysis of the density for both the NCS and traditionally symmetrized maps, which indicated that the loop is more ordered after acetylation. The residual disorder identified by the simulations using the $Ac^{96}$ map may be
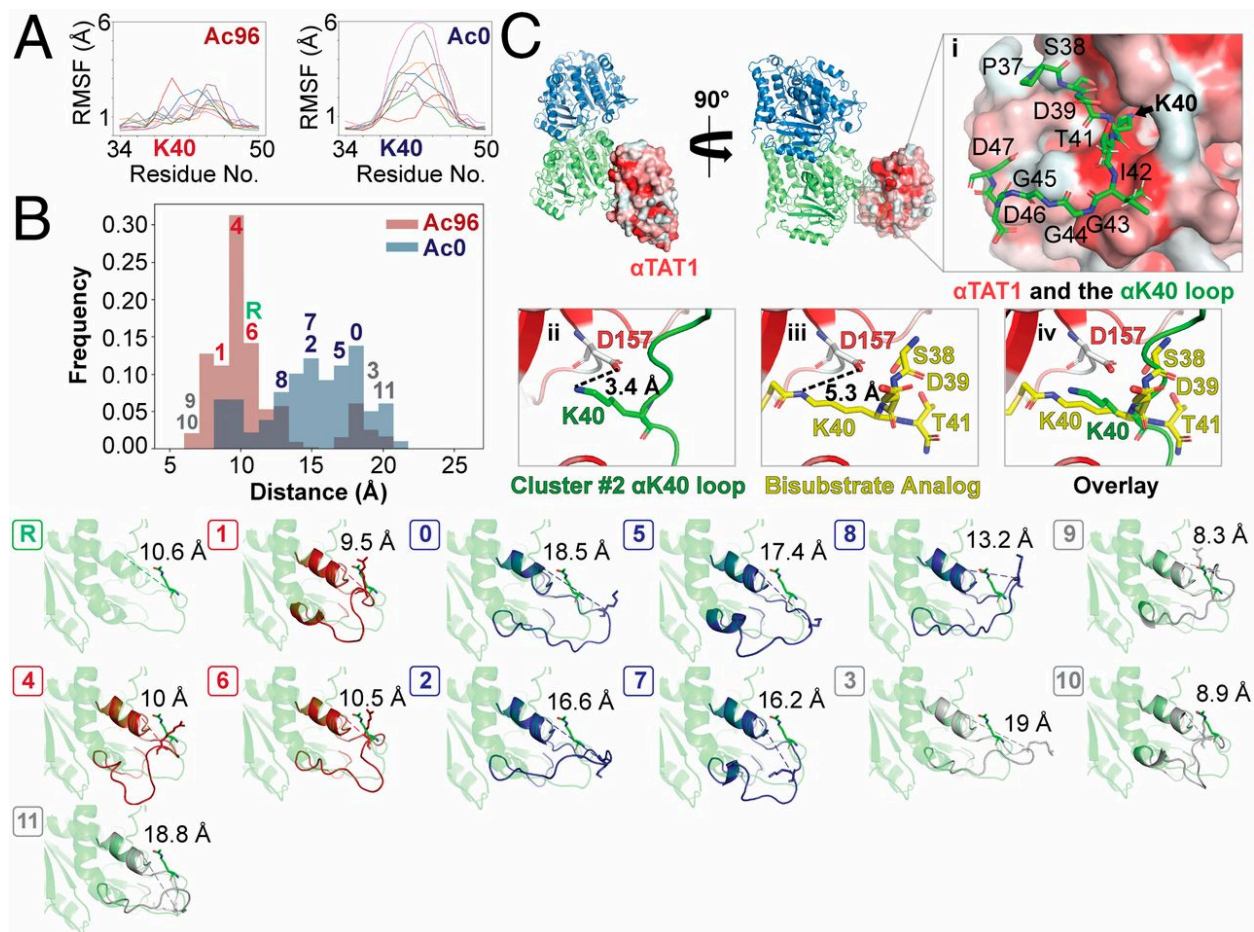


**Figure 10** | Acetylation restricts the motion and alters the conformational ensemble of the αK40 loop. (A) Per-residue root-mean-square fluctuation (RMSF) analyses were determined over the course of 12 ns for residues 34–50 the C1 maps using GROMACs in PLUMED and graphed using the MDAnalysis. The different colored lines refer to the eight different replicas. (B) Ensemble modeling of the loop across Ac96 and $Ac^0$ states using density restrained MD. Frames were classified into 1 of 11 clusters by conformation. Clusters either had a greater number of $Ac^{96}$ frames (red), $Ac^0$ frames (blue), or an equal number of frames from both states (gray). The reference is shown in green. The unique conformations of each of the 12 clusters (0–11) are shown below. (C) αTAT1 cocrystalized with a bisubstrate analog consisting of α-tubulin residues 38–41 (PDB ID code 4PK3) is shown bound to αβ-tubulin sampling the αK40 loop of cluster 2 from the metainference ensemble. αTAT1 is colored by hydrophobicity, where hydrophobic regions are red. (C, i) After backbone alignment of the surrounding residues of the bisubstrate analog, αK40 from cluster 2 fits directly into the catalytic groove, highlighted by the black arrow. (C, ii–iv) Similar to the bisubstrate analog (shown in yellow), αK40 from the

important for deacetylation by SIRT2. On the other hand, the increased flexibility we observe for the Ac[0] state suggests a potential mechanism by which αTAT1 could acetylate K40. Previous proposals argued that acetylation can occur from the outside[63] or inside of the lumen[43]. However, to catalyze the modification, a flexible region within αTAT1 would have to extend ~25 Å through a MT wall fenestration between four tubulin dimers to reach αK40, or the MT would have to undergo a major structural rearrangement in the lattice to allow αTAT1 to enter the lumen. Previous work demonstrated that the αTAT1 active site and its MT recognition surface is concave and could not stretch through the lumen[43,44]. Our findings support the idea that αTAT1 modifies the loop from within the lumen of the MT because the deacetylated loop samples extended structures that could be accessible to αTAT1 and because the structural rearrangement caused by acetylation is small and local to the αK40 loop.

To test this idea, we superposed the backbone of the bisubstrate analog consisting of α-tubulin residues 38–41 from the αTAT1 cocrystal structure (PDB ID code 4PK3) with representatives of the clusters from the metainference ensemble. Not surprisingly, most arrangements generated severe clashes between αTAT1 and the globular domain of α-tubulin. However, the model from cluster 2 had only a single severe clash (between αTAT1:R74 and α-tubulin:G57) and displayed reasonable surface complementarity with αTAT1, positioning αK40 directly into the catalytic groove (Fig. 10C, i). Here, αK40 remains within a close proximity of αTAT1:D157 (Fig. 10C, ii–iv), which coordinates an essential hydrogen-bond network at the enzyme–tubulin interface and when mutated decreases acetylation by ~96% and ~92% for free tubulin and within assembled MTs, respectively[43]. Notably, although cluster 2 was not the most extended conformation, it was highly enriched in the Ac[0] ensemble. This finding bolsters the model that acetylation occurs from inside the lumen[43] and suggests that deacetylated α-tubulin samples the conformations that are competent for catalysis by αTAT1 with relatively little energetic cost.

## 2.1.4 Acetylation induces a local structural rearrangement of the αK40 loop that promotes stability by weakening lateral contacts

Collectively our structural and MD results show that acetylation restricts the motion of the αK40 loop. These results led us to hypothesize that the change in the structural ensemble of the αK40 loop upon acetylation, while subtle and local, may affect lateral contacts. These local changes may disrupt the small lateral interface between α-tubulin subunits. The origin of this effect may be highly distributed, as we do not visualize any stable interactions between the $Ac^0$ state of the loop and the globular domain. However, upon acetylation, the structural ensemble becomes more restricted and the potential for the loop to strengthen any of these interactions between monomers is lost. For example, in many of the extended conformations favored by the $Ac^0$ state, K40 in a α1-monomer is close to the M-loop of the neighboring α2-monomer and may buttress the H1′–S2 loop, providing support for the vital α1K60:α2H283 lateral interaction (Fig. 11). In contrast, when K40 is acetylated, it packs ∼10 Å closer to the globular domain of the α1-monomer, reducing the potential for intermonomer interactions (Fig. 11).

We tested whether K40 acetylation alters the electrostatic interaction energy and the hydrogen-bonding network at the lateral interface by estimating the electrostatic interactions. We used the Debye–Hückel (DH) formula to calculate interaction energies for each conformation sampled in the two metainference ensembles and compared the resulting distributions. We found that acetylation does indeed weaken lateral interactions.
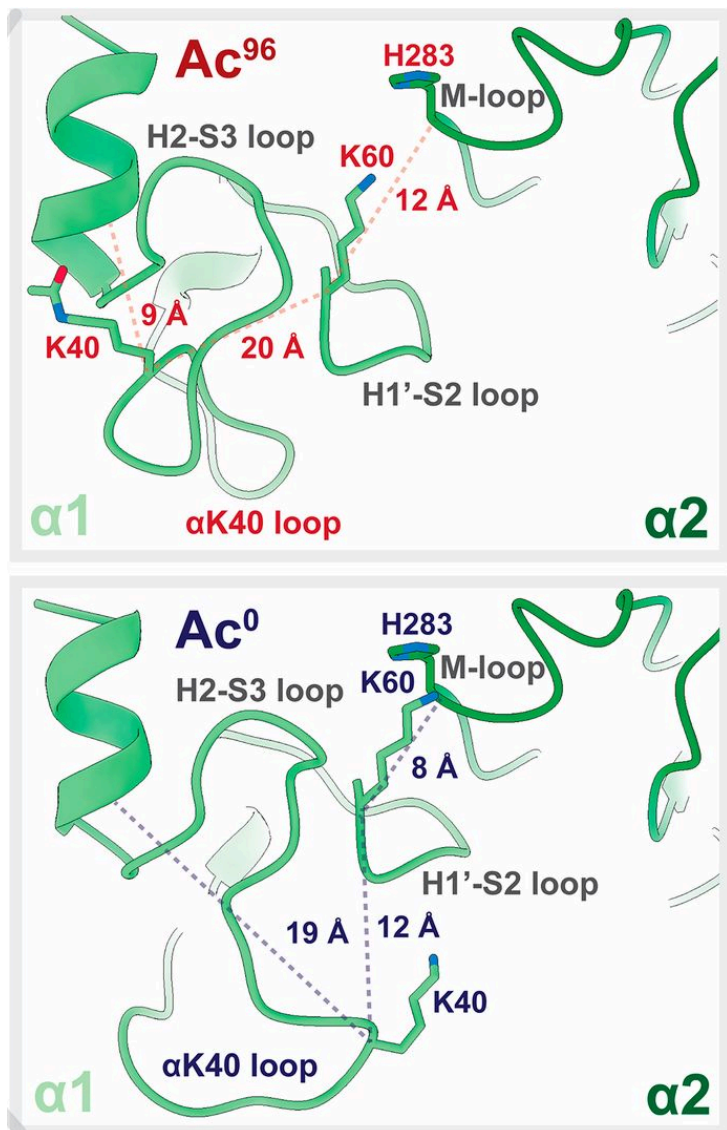


**Figure 11** | Acetylation may weaken lateral interactions. Close-up view of the lateral contacts between two α-tubulin monomers at a nonseam location (α1, light green; α2, dark green). K40 in α1 of the $Ac^0$ state is 8 Å closer to the M-loop of α2 and appears to buttress the H1′–S2 loop, providing support for the vital α1K60–α2H283 lateral interaction. By contrast, that support is lost in the $Ac^{96}$ state because the acetylated K40 now packs much closer to the hydrophobic, inner core.

Additionally, the Ac$^0$ ensemble contains conformations with strong DH interaction energies that do not exist in the Ac$^{96}$ ensemble (See Fig. S5 in Eshun-Wilson et al. PNAS, 2019 for more details). While the effects of acetylation are subtle, the local effects at the lateral contacts site may have an additive effect that stabilizes the MT lattice. This idea is consistent with previous work that argues that the weakening of lateral interactions is a protective mechanism to prevent preexisting lattice defects from spreading into large areas of damage under repeated stress—a mechanism that could be exploited by cancer cells[3,40,64].

In conclusion, this integrative approach combines the structural insight of cryo-EM with the sampling efficiency of MD to investigate how PTMs can transform a conformational ensemble. Our high-resolution maps serve as a blueprint for the scale of conformational change and relevant degrees of freedom that the αK40 loop can sample. We show that acetylation of tubulin induces electrostatic perturbations that restrict the motion of the αK40 loop, weakening lateral contacts. The sum of many weak reduced lateral contacts reduces the inter-PF interactions. The increased flexibility provided by fewer inter-PF interactions provides a mechanism by which αTAT1 can locally fine-tune the load-bearing capacity and mechanical resistance to stress of MTs[64,65]. Deacetylation increases lateral contacts, which renders MTs inflexible, brittle, and highly susceptible to breakage under stress[64]. The pattern of increased lateral interactions between subunits leading to mesoscale instability may be conserved in other polymeric systems[66,67]. Therefore, αK40 acetylation may function as an evolutionarily conserved "electrostatic switch" to regulate MT stability[68,69]. Cancer cells may exploit this subtle form of regulation to promote cell adhesion, invasive migration, and other markers of aggressive metastatic behavior[36].

## 2.2. Materials and Methods

This chapter outlines the necessary methods for our structural interpretation. Didier Portran performed the tubulin purification and modification to generate the $Ac^0$ and $Ac^{96}$ samples. Lisa Eshun-Wilson and Rui Zhang performed the cryo-EM sample preparation, electron microscopy and data processing. Lisa Eshun-Wilson and Jamie Fraser engineered the NCS-averaging technique, performed iterative model-building/refinement. Lisa Eshun-Wilson, Jamie Fraser, Massimiliano Bonomi and Michele Vendruscolo executed the metainference MD simulations. All authors contributed to structure interpretation, model development and manuscript writing.

### 2.2.1 Sample preparation for cryo-electron microscopy

Porcine brain tubulin was purified as previously described[70] and reconstituted to 10 mg/mL in BRB80 buffer [80 mM Pipes, pH 6.9, 1 mM ethylene glycol tetraacetic acid (EGTA), 1 mM MgCl2] with 10% (vol/vol) glycerol, 1 mM GTP, and 1 mM DTT, and flash-frozen in 10-µL aliquots until needed. The acetylated and deacetylated MTs (15 µM) were copolymerized with EB3 (25 µM), at 37 °C for ~15 min in the presence of 10% Nonidet P-40, 1 mM DTT, and BRB80 buffer. The EB3-decorated MTs were added to glow-discharged C-flat holey carbon grids (CF-1.2/1.3–4C, 400 mesh, copper; Protochips) inside a Vitrobot (FEI) set at 37 °C and 85% humidity before plunge-freezing in ethane slush and liquid nitrogen, respectively, as previously described[9].

### 2.2.2 Cryo-electron microscopy

Micrographs were collected using a Titan Krios microscope (Thermo Fisher Scientific) operated at an accelerating voltage of 300 kV. All cryo-EM images were recorded on a K2 Summit direct electron detector (Gatan), at a nominal magnification of 22,500×, corresponding to a calibrated pixel size of 1.07 Å. The camera was operated in superresolution mode, with a dose rate of ~2 e– per pixel per s on the detector. We used a total exposure time of 4 s, corresponding to a total dose of 25 electrons/Å2 on the specimen. The data were collected semiautomatically using the SerialEM software suite[71]. See data collection tree below in Fig. 12.

### 2.2.3 Image processing

Stacks of dose-fractionated image frames were aligned using the UCSF MotionCor2 software (47). MT segments were manually selected from the drift-corrected images (acetylated dataset, 205 images; deacetylated MT dataset, 476 images) using the APPION image processing suite (48). We estimated the CTF using CTFFIND4[72] and converted the segments to 84% overlapping boxes (512 × 512 pixels) for particle extraction. The remaining nonoverlapping region is set to 80 Å and corresponds to the tubulin dimer repeat (asymmetric unit). Consequently, there are ~13 unique tubulin dimers per MT particle. To determine the initial global alignment parameters and PF number for each MT particle, raw particles were compared with 2D projections of low-pass filtered MT models (~20 Å, 4° coarse angular step size) with 12, 13, 14, and 15 PFs using the multireference alignment (MSA) feature of EMAN1[50].
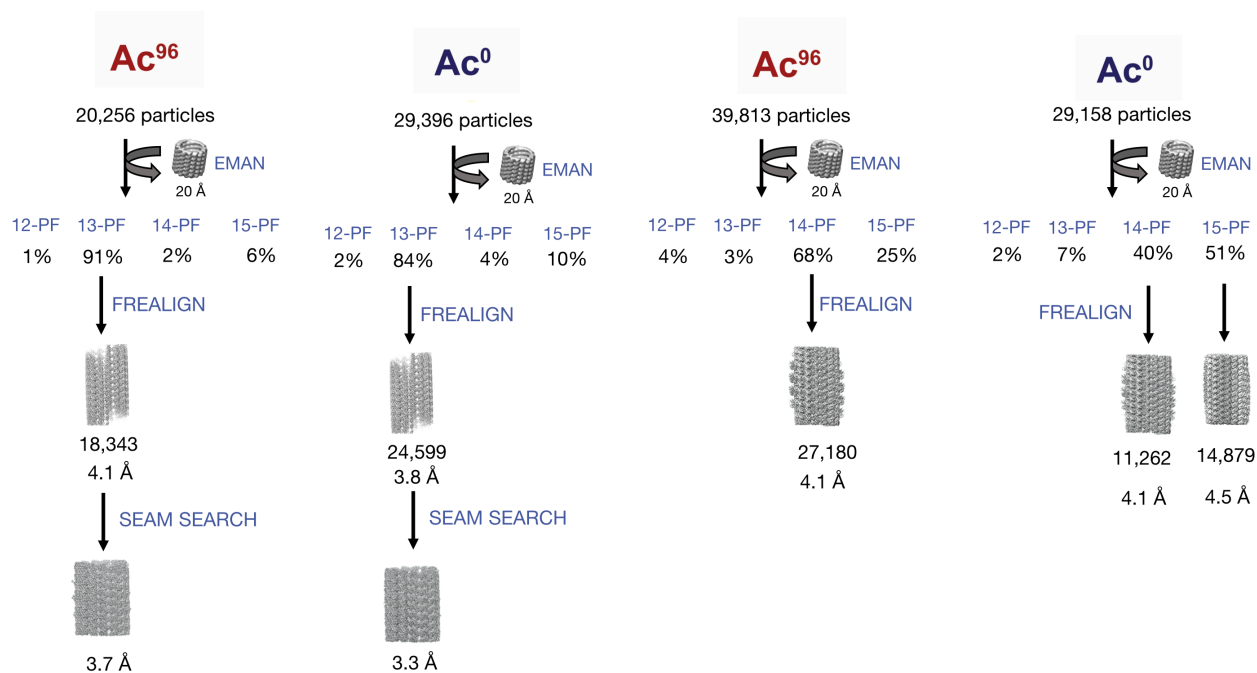
**Figure 12** | Data collection tree for acetylated and deacetylated MTs in the presence of EB3 and kinesin.

Finally, 13-PF MT particles (acetylated dataset, 20,256 particles; deacetylated MT dataset, 29,396) were refined in FREALIGN, version 9.11[52], using pseudohelical symmetry to account for the presence of the seam. To verify the location of the seam, we used the 40-Å shift approach to categorize MTs based on their azimuthal angle, as previously described[54]. See the data collection tree below (Fig. 12).

## 2.2.4 Atomic model building and refinement

COOT[73] was used to build the missing polypeptides of the αK40 loop in α-tubulin, using the available PDB 3JAR as a starting model. Successively, all ab initio atomic models were iteratively refined with phenix.real_space_refine into EM maps sharpened with phenix.autosharpen (29, 55). For visual comparisons between states, potential density thresholds were interactively adjusted in Coot to maximize isocontour similarity around backbone atoms distant from the αK40 loop. For Figs. 8 and 9, all densities are represented in Chimera at a threshold of 1.1.

## 2.2.5 Molecular dynamics simulations

Code for map preparation, simulation execution, and analysis is available at https://github.com/fraser-lab/plumed_em_md.

To prepare the cryo-EM maps, we fitted the maps with a Gaussian mixture model (GMM) by applying a divide-and-conquer approach[62], using generate_gmm.py and convert_GMM2PLUMED.sh. Cross-correlations to the experimental maps were greater than 0.99. All simulations were performed with GROMACS 2016.5[74] and the PLUMED-ISDB[75] module of the PLUMED library[76] using the Charmm36-jul2017 forcefield[77] with patches for acetylated lysine (aly)[78] and the TIP3P water model. For the deacetylated simulations, the same starting model was used with a manual edit of the PDB to eliminate the acetylation (with all hydrogens replaced by GROMACS during model preparation). The initial model was minimized then equilibrated for 2 ns, using prep_plumed.py. MD simulations were performed on a metainference ensemble of eight replicas for an aggregate simulation time of 96 ns for each acetylation state, using prep_plumed2.py and prep_plumed3.py. Contributions of negative scatterers (atoms OD1 and OD2 of Asp residues; OE1 and OE2 of Glu) were excluded from contributing to the predicted maps during the simulation. This modification effectively eliminates the contribution of these side chains to the agreement between density maps, in keeping with the nonexistent density of negatively charged side chains in EM maps, while allowing them to contribute to the simulation through the energy function. Clustering and convergence analyses[60] were performed and analyzed using MDAnalysis[79].

Clustering of the two metainference ensembles was carried out using the Gromos method[80] after aggregating the trajectories of the $Ac^0$ and $Ac^{96}$ simulations. A subset of every 10 frames were selected from the entire aggregated trajectory. The distance between two conformations was defined as the RMSDs calculated on the Cα atoms of the αK40 loop. The clustering cutoff was equal to 2.5 Å, with similar results obtained with other cutoffs. The population of each cluster in the $Ac^0$ and $Ac^{96}$ ensembles was then recalculated from the two separate trajectories. Changes in the electrostatic interaction energies at the lateral contacts were determined using the using the DH formula. Parameters used in the calculation of the DH energy are as follows: temperature (T = 300 K), dielectric constant of solvent ($\epsilon_r$ = 80; water at room temperature), and ionic strength ($I_S$= 0.3–1 M).

**Accession Numbers.** All electron density maps have been deposited in the Electron Microscopy Data Bank, www.ebi.ac.uk/pdbe/emdb/ (EMDB ID codes EMD-0612, EMD-0613, EMD-0614, and EMD-0615). Atomic models have been deposited in the Protein Data Bank, www.wwpdb.org (PDB ID codes 6O2Q, 6O2R, 6O2S, and 6O2T).

Chapter 3: Effects of the therapeutic agent Lankacidin C (LC) on MT function and ribosome activity

3.1 Results and discussion

Similar to PTMs and MAPs, therapeutic agents can affect MT structure and stability. Taxol, a major breast cancer chemotherapy agent, blocks the cell cycle in its G1 or M phases by stabilizing MTs and limiting MT depolymerization[6]. This chapter discusses the effects of Lankacidin C (LC), an antibiotic with in vivo antitumor activity in multiple cancer cell lines and antimicrobial activity against Gram-positive pathogens on MT structure. We observed that LC did not polymerize MTs in a taxol-like manner and the hypothesized in vivo antitumor activity in likely due to the previous lack of the proper experimental controls. Based on this finding, we shifted our focus to the effects of LC on bacterial translation and its role as an antibiotic. We present a 2.8 Å structure of the LC-ribosome complex, which improves upon the existing model and shows that LC ring closure is imperative for its mechanism of action. This mechanism may be conserved across related metabolites in the lankacidin class for their antibiotic activity. Ian B. Seiple performed the lankacidin isolations/syntheses and Fred Ward performed the bacterial ribosome purification. Jenna Pellegrino performed the in vitro translation assays. Lisa Eshun-Wilson performed the cryoEM sample preparation, data collection, and data processing. Collectively, Lisa Eshun-Wilson, D. John Lee, Jenna Pellegrino, Dan Toso and Jaime Fraser completed the cryo-EM sample preparation, data collection and data processing and analysis. All authors contributed to structure interpretation, model development and manuscript writing.

3.1.1 Turbidity assays debunk the previous hypothesis that lankacidin stabilizes MTs and has anti-tumor activity

Isolated for the first time in 1969, lankacidin-group antibiotics (T-2636) are fermentation products that are produced by the organism Streptomyces rochei, see 4.2.1. for more details. The parent of this group Lankacidin C (LC), a 17-membered macrocyclic tetraene, shows strong antimicrobial activity against multiple Gram-positive bacteria, even those highly resistant to macrolide antibiotics, such as X and Y, making them popular in veterinary medicine[81]. The antimicrobial mechanism of action of lankacidin is due to interference with peptide bond formation during protein synthesis by binding at the peptidyl transferase center (PTC) of the eubacterial large ribosomal subunit, discussed in more detail in 4.1.2.

In addition to its antimicrobial activity, scientists believed LC and its derivatives possessed antitumor activity. Most antibacterial antibiotics had proven ineffective chemotherapy agents against mammalian tumors, until 1973, when LC, LC 8-propionate (LC8) and LC 14-propionate (LC14) were shown to effectively retard tumor growth in mice[82]. Each metabolite was administered intraperitoneally at doses 25 to 1000 mg/kg to suppress the following tumors: leukemia L-1210, lymphosarcoma 6C3HED/OG sensitive to l-asparaginase and melanoma B-16 in mice. At high doses, LC suppressed the production of antibodies against erythrocytes in mice, both before and after antigenic simulation, though, LC8 and LC14 exhibited significant but weak effects on tumor growth. Additional studies later on showed that

by replacing the hydroxyl group at position 8 or 14 of LC with an acyloxy group instead of propionate group, enhanced their respective antitumor activity against L1210 leukemia and 6C3HED/OG lymphosarcoma[83].

The mechanism of action for the proposed antitumor activity of LC remained elusive, however, until 2016, when Ayoub et al. conducted turbidity assays to show that LC increased the rate of tubulin assembly comparable to taxol, or paclitaxel[84]. They concluded that LC bound MTs to stabilize and halt MT dynamics in a paclitaxel-like manner. In addition to turbidity assays, competitive binding assays found that LC competed with the fluorescent taxoid flutax-2 for the paclitaxel binding site, with a weak dissociation constant of $K_d$ of 50 ± 13 μM. Moreover, fluorescence quenching assays revealed that LC bound to assembled tubulin with a greater affinity than to free dimers. The authors also conducted molecular dynamics simulations LC bound to the paclitaxel-binding site of β-tubulin to estimate the binding energy between LC and tubulin.

We set out to confirm previous work that asserts LC binds MTs in a paclitaxel-like manner. We began by repeating the tubulin polymerization assay (Cytoskeleton, Inc., catalog no. BK006P), based on the principle that MT solutions scatter light in a concentration dependent manner[85]. In this assay, MT growth is tracked by measuring the optical density of the solution at 340 nm over time. To illustrate this point further, a tubulin growth curve shows tubulin polymerization at multiple conditions over the course of three phases: (1) lag, (2) growth, and (3) steady state[86,87] (Fig. 13).



Figure 13 | A tubulin polymerization assay measures optical density as a function of time. This assay allows to probe how different conditions change the three stages of MT dynamics: (1) lag, or the initial stage in which MTs begin to nucleate; shown in red (2) growth, or the linear stage in with MTs begin to elongate; shown in orange (3) steady state, or the saturating stage shown in green.

Experimentally, in the presence of GTP, tubulin remains in the lag phase for ~10 min before entering the growth phase and, finally, saturating at an OD340 of 0.4 (Fig. 14). In the presence of MT-stabilizer paclitaxel at concentrations of 1 μM and 10 μM, tubulin immediately begins to elongate into MTs, bypassing the lag phase, and saturating at a higher OD340 of 0.73 and 0.82, respectively, due to the higher final polymer mass (Fig. 14). These controls yielded the expected results and therefore validate the tubulin polymerization assay as an effective tool to test the effects of a MT-stabilizing compound on MT dynamics. Next, we measured the effects of dimethyl sulfoxide (DMSO) and LC on MT polymerization in a dose-dependent manner. DMSO has a significant effect on MT polymerization and dynamics. In 1988, it shown that DMSO lowered the critical concentration of tubulin 10-fold, from 9.4 μM in the absence of the organic solvent to 1.1 μM in its presence[87].
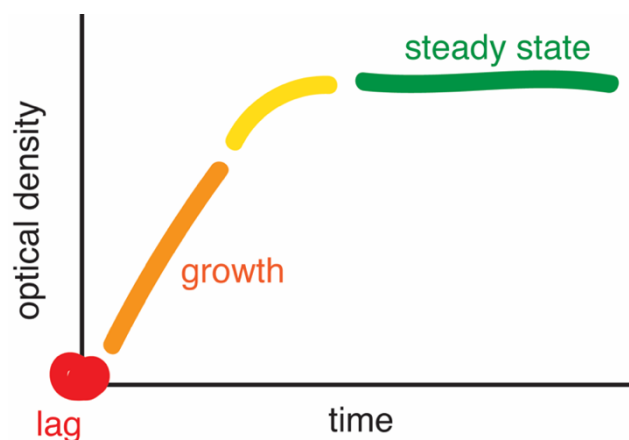
Thus, it is imperative to deconvolute the effects of small molecules in solution with DMSO when measuring their effect on MT polymerization.

We compared the effects of paclitaxel, LC solutions and DMSO on MT polymerization not only at multiple concentrations but also in distinct buffer conditions: either in 99% DMSO solution or 1xBRB80 containing GTP (Buffer Mix), for more details visit 4.2.2. In the presence of 10 µM LC in DMSO, while the nucleation phase is shortened and the reaction enters the steady state phase at 0.68, this growth curve is not significantly different from that of the 100% DMSO solution (Fig. 14). Moreover, the effects of LC in DMSO at a concentration of 100 µM (black triangle) are less significant than that of paclitaxel in DMSO at 1 µM (blue cross). We observe the effects of LC scale proportionately with those of DMSO. Whereas, Ayoub et al. found that 10 µM LC entered the steady state at the same point (0.33) as the 10 µM paclitaxel condition and the GTP only condition, which is problematic. Our polymerization assay thus supports that the effects of LC on MT polymerization and stability are insignificant. We hypothesize that LC does not confer MT stability in a paclitaxel-like manner and the observed antitumor activity of LC may be due to the presence of DMSO. Ayoub et al. also point out the predicted affinity of LC for the paclitaxel binding site does not necessary correlate with the potency of the drug as a cytotoxic agent. If LC does possess antitumor activity, it's mechanism of action may involve different cellular targets or cytotoxic effects.
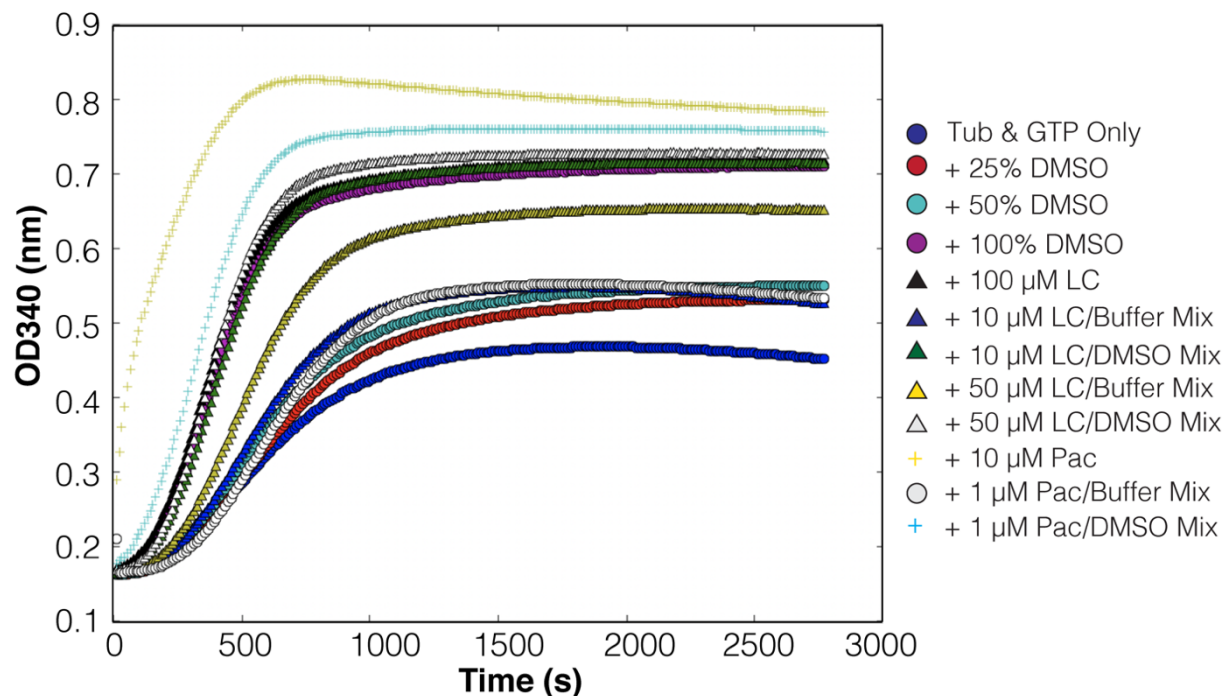


Figure 14 | Tubulin polymerization curves at varying conditions. Polymerization is monitored by measuring the optical density at 340 nm versus time. The plots show polymerization without DMSO or a MT-stabilizing agent (LC or Pac), with varying amounts of DMSO (25%, 50%, and 100%), with varying amounts of Lankacidin C (LC; 10 µM, 10 µM,100 µM) resuspended in either DMSO or buffer (1xBRB80), or with varying amounts of Paclitaxel (Pac; 1 µM,10 µM).

### 3.1.2 High-resolution cryo-EM reconstructions of lankacidin-bound ribosomes

Based on our findings in 4.1.1, we decided to shift our focus on elucidating LC's mechanism of action for its antimicrobial activity. A previously published 3.5 Å resolution X-ray crystallography structure of the large ribosomal subunit from *Deinococcus radiodurans* (D50S) in complex with LC provided the first insight into the location of LC in the peptidyl transferase center (PTC), a highly conserved region of the ribosome[88]. Based on this structure it was predicted that LC forms extensive interactions with nucleotides A2602, C2452, A2503, U2504, G2505, U2585, G2061, and U2506 in the PTC. With our improved resolution, we find, however, that LC forms hydrophobic contacts with A2451 instead of A2602 (Fig. 15).

Here, we present a 2.8 Å structure of the LC-ribosome complex and, consistent with the previous structure, we find that specific oxygen molecules within LC are ~3.3 Å, or the distance of a hydrogen bond, away from the following nucleotides and forms hydrogen bonds with: N1 and N2 of G2061, 2'OH of A2503, and O5' of G2505 (Fig. 15E and F). We can now observe density for these hydrogen bonds and the hydrophobic contacts LC makes with A2451, C2452, A2503, U2504, G2505, U2585, G2061, and U2506 (Fig. 15A) compared to that of the previous structure (Fig. 15B). Our structure further supports that LC takes advantage of the flexibility of the PTC and blocks the 3'end of the tRNA molecule in the aminoacyl site or A-site of the ribosome, thus preventing the tRNA from binding a new amino acid through its acceptor stem and halting translation.
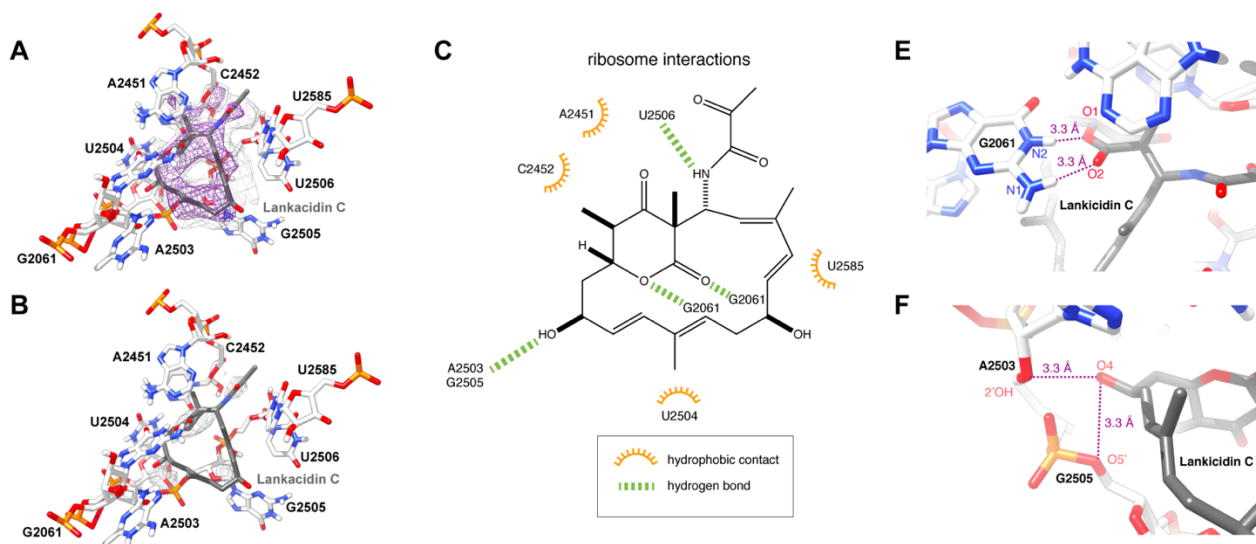


**Figure 15 |** Synthetic Lankacidin C and its molecular mechanism of action. Cryo-EM maps of Lankacidin C in the peptidyl transferase center (PTC) of the 70S subunit of the *E. coli* ribosome 2.8 Å (A) and at 3.5 Å (B; Auerbach, PNAS, 2010). Coulomb potential density is contoured in light gray at 2.0 and purple at 7.0 in Chimera. (C) Graphical representation of interactions between LC and residues in the ribosomal binding site. Hydrogen-bond network between O1 and O2 of LC with N2 and N1 of G2061, respectively, and (E) between O4 and 2'OH of A2503 and O5' G2505 (F).

This elaborate hydrophobic network that LC forms within the PTC pocket is essential for its inhibitory effect on translation and common for this class of macrolides[89]. Previous work found that hydrogenation of the macrocyclic ring alters its ring conformation and reduces the inhibitory activity of LC[89]. Bacteria may resist LC over time by manipulating the identity of these nucleotides, so as not lethally affect ribosome function, but weaken LC binding to the PTC site. We also see the 2-methyl group at the lactone edge of the macrocyclic ring insert into the opening of the hydrophobic crevice formed by A2451 and C2452, as previously shown, which enables LC to compete multiple other antibiotics that target the aminoacyl moiety of the A-site that bind aminoacyl-tRNAs (aa-tRNAs or charged tRNAs)[90,91].

### 3.1.3 In vitro translation assay of Lankacidin C

In line with our structural evidence, we found that LC inhibited 70S *E. coli* translation with an $IC_{50}$ of 4.31 µM +/- 0.1, higher than the previously reported value of 1.5 ± 0.1 µM[90] (Fig. 16). This result supports LC as an effective inhibitor of bacterial translation.
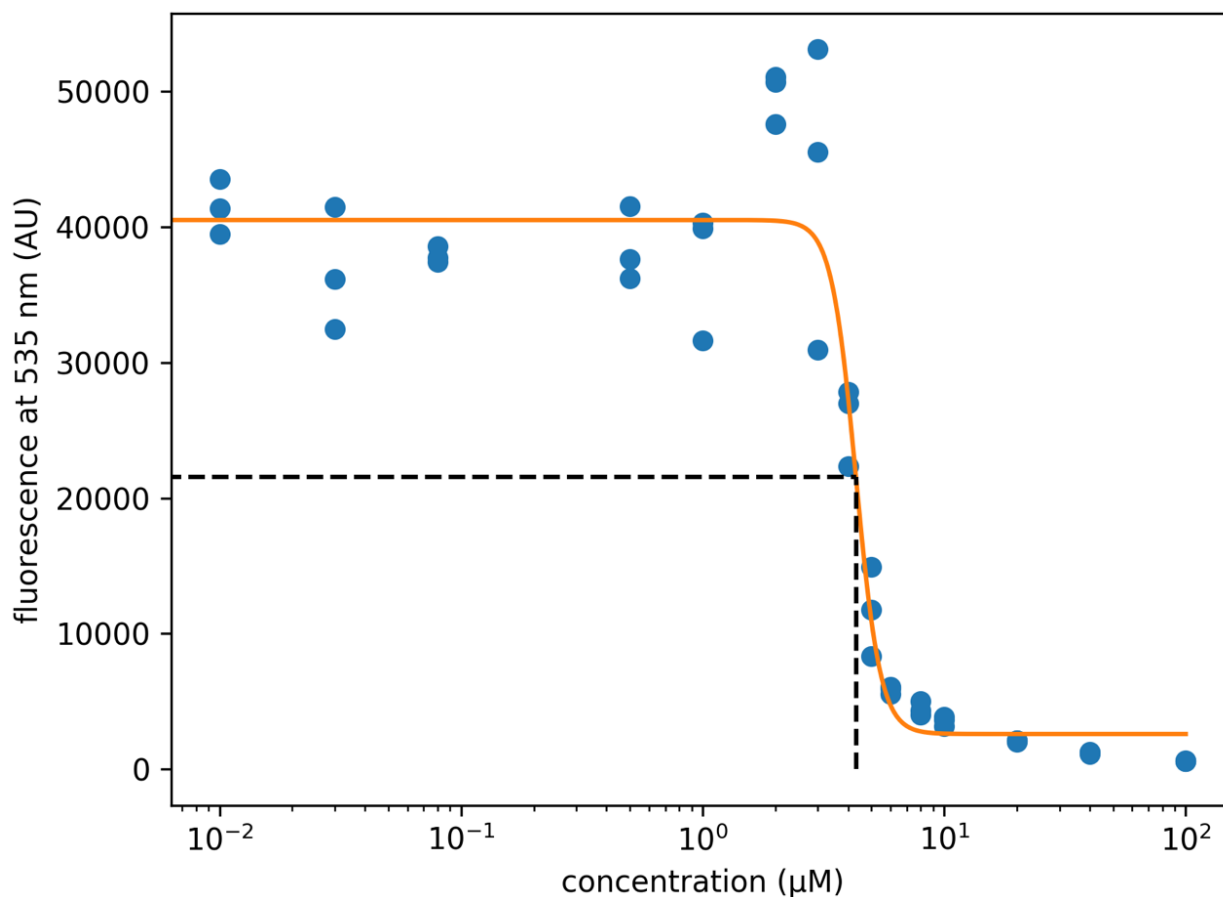


Figure 16 | Cell-free dose response curve for lankacidin C (LC) inhibition of 70S *E. coli* translation. Plotted data points come from the normalized averages of two experimental triplicates. Dashed lines guide the eye to the inflection point of the sigmoid, where the IC50 of LC is exhibited at 4.31 µM +/-

Our MT polymerization assays and cryo-EM data show that LC exhibits strong antimicrobial activity, as previously established, but, possibly not antitumor activity. Based on our MT polymerization assays, we hypothesize that LC does not confer MT stability in a paclitaxel-like manner and the observed antitumor activity of LC may be due to the presence of DMSO. In addition, our 2.8 Å cryo-EM map improves upon the existing model and allows us to more confidently identify contacts LC makes with the PTC.

## 3.2. Materials and Methods

### 3.2.1 Metabolite Isolation

*S. rochei* strain 51252 was cultured in YM media (2 L) at 28 °C for 2 days. The culture broth was added to a 3-L separatory funnel and was extracted with ethyl acetate (3 x 500 mL). The organic layers were combined, and the resulting suspension was washed with sat. aqueous sodium chloride (500 mL). The washed organic solution was dried with sodium sulfate, the mixture was filtered, and the filtrate was concentrated under reduced pressure. The resulting residue was purified by column chromatography on silica gel (eluant: 2% → 10% methanol in chloroform) to provide lankacidin C (3.3 mg) as a white solid. The spectroscopic data matched the previously reported data (Chem. Biol. 2005, 12, 249-256).

### 3.2.2 Sample purification

*E. coli* strain MRE600 overnight cultures were diluted 1:100 into 3 L of LB. After growth to mid-log phase (OD 0.6), cells were cooled on ice for 3 min, pelleted, and washed with buffer A (20 mM Tris-HCl pH 7.5, 100 mM $NH_4Cl$, 10 mM $MgCl_2$, 0.5 mM EDTA, 2 mM DTT). Cells were resuspended in 100mL buffer AS (buffer A with 0.15 M sucrose) and lysed with two passes through an Emulsiflex-C3 homogenizer at 18000 psi. Lysate was clarified by centrifugation for 30 min at 18000 rpm in a JA-20 rotor (Beckman-Coulter). The supernatant was layered over a sucrose cushion of 24 mL buffer B (buffer A with 500 mM $NH_4Cl$) with 0.5 M sucrose and 17mL buffer C (20 mM Tris-HCl pH 7.5, 60 mM $NH_4Cl$, 6 mM $MgCl_2$, 0.5 mM EDTA, 2mM DTT) with 0.7 M sucrose in ti-45 tubes (Beckman-Coulter). Ribosomes were pelleted in a Ti-45 rotor at 27000 rpm for 16 hours at 4 °C. Crude ribosome pellets were resuspended in disassociation buffer (buffer C with 1mM $MgCl_2$) and clarified via centrifugation at 15000 g for 10 min. The cleared supernatant was layered over 15-40% sucrose gradients in disassociation buffer and spun 28000 rpm for 16 hours at 4 °C in a SW-32 rotor (Beckman-Coulter). Gradients were fractionated with an ISCO fractionation system and 30S + 50S peaks were combined. The combined subunits were concentrated in 15 mL Millipore 100k molecular weight cutoff spin filter and buffer exchanged with reassociation buffer (buffer C with 10 mM $MgCl_2$). Ribosomes were incubated 45 min at 37 °C, layered onto 15-40% sucrose gradients in reassociation buffer, and spun 27000 rpm for 15 hours at 4 °C in an SW-32 rotor. Gradients were fractionated as before, 70S peaks were collected, and ribosomes were concentrated and washed with buffer C in an Amicon stirred cell filtration system using 100k cutoff filters. Ribosomes were stored in aliquots at -80 °C.

### 3.2.3 In vitro translation assays

Lankacidin C (LC) inhibition of 70S *E. coli* translation was tested in a cell-free system as described in Li et al. with the following differences. The in vitro translation assay was performed at a concentration range of 0.01 to 100 µM LC in 10% DMSO. Reactions were performed in technical triplicate and in biological duplicate. For each biological replicate, the fluorescence readouts were averaged across the triplicates. The data were normalized relative to the average

fluorescence of the 0-LC control. The IC50 was interpreted from these data, as previously described[92].

### 3.2.4 Tubulin turbidity assays

Porcine brain tubulin was purchased from Cytoskeleton, Inc., reconstituted to 10 mg/ml in BRB80 buffer (80 mM 1,4-piperazinediethanesulfonic acid [PIPES], pH 6.9, 1 mM ethylene glycol tetraacetic acid [EGTA], 1 mM MgCl2) with 10% (vol/vol) glycerol, 1 mM guanosine triphosphate (GTP), and 1 mM dithiothreitol [DTT], and provided to us by the Ron Vale lab. 10 μL reactions of paclitaxel solution, lankacidin solutions, dimethyl sulfoxide (DMSO) with and without GTP (as positive controls) or buffer solutions (as a negative control) were added to 10 μL of tubulin in a buffer. This resulted in 9 samples having final concentrations of 10 μM paclitaxel, 10 μM lankacidin C, 10 μM lankacidin A, or a negative control, all dissolved in a solution containing final concentrations of 3 mg/mL tubulin, 80 mM PIPES, pH 6.9, 2 mM MgCl2, 0.5 mM EGTA, and 1 mM GTP. The plate was immediately placed in a 37 °C prewarmed 384-well plate (Corning, Inc., Lot. No. 34214031) to follow MT growth through optical density over the course of 30 min. The experiment was repeated in triplicate and the average curve of OD340 versus time was plotted, and parameters were studied.

### 3.2.5 Sample preparation for cryo-EM

Ribosomes were prepared at a concentration of 3.4 μM in a buffer of 50 mM HEPES, 150 mM KOAc, 6 mM Mg(OAc), 7mM β-mercaptoethanol (BME) and 0.01% NP-40 and treated with 100 nM Lankacidin in 1% DMSO. Samples were plunge-frozen on glow-discharged C-flat holey carbon grids (CF-2/2-4C, 400 mesh, Copper; Protochips, Morrisville, NC) inside a Vitrobot (FEI, Hillsboro, OR) set at 22 °C with 100% humidity and a blot force of 0, blot time of 0 sec before plunge-freezing in ethane slush and liquid nitrogen.

### 3.2.6 Cryo-EM

Micrographs were collected using a Titan Krios microscope (FEI, Hillsboro, OR) operated at an accelerating voltage of 300 kV. All cryo-EM images were recorded on a K2 Summit direct electron detector (Gatan, Pleasanton, CA), at a nominal magnification of 105000 corresponding to a calibrated pixel size of 1.059 Å. The camera was operated in super-resolution mode, with a dose rate of 5.42 to e- per pixel per s on the detector camera. We used a total exposure time of 9 s, corresponding to a total dose of 45 electrons/Å2 on the specimen. The data were collected semi-automatically using the SerialEM software suite[71].

## 3.2.7 Image Processing

Movies were motion corrected using MotionCorr2 and then imported into cisTEM. CTF estimation and particle picking were performed using default parameters except maximum particle radius 120 Å and characteristic particle radius 80 Å, resulting in 87706 picked particles. Twenty rounds of 2D classification into 60 classes, removing suboptimal particles, resulted in 41221 particles, which were used for ab initio 3D reconstruction. This procedure resulted in a 3.3 Å reconstruction. Further 3D classification generated a 2.8 Å reconstruction when CTF refinement was included, which was sharpened using the default parameters.
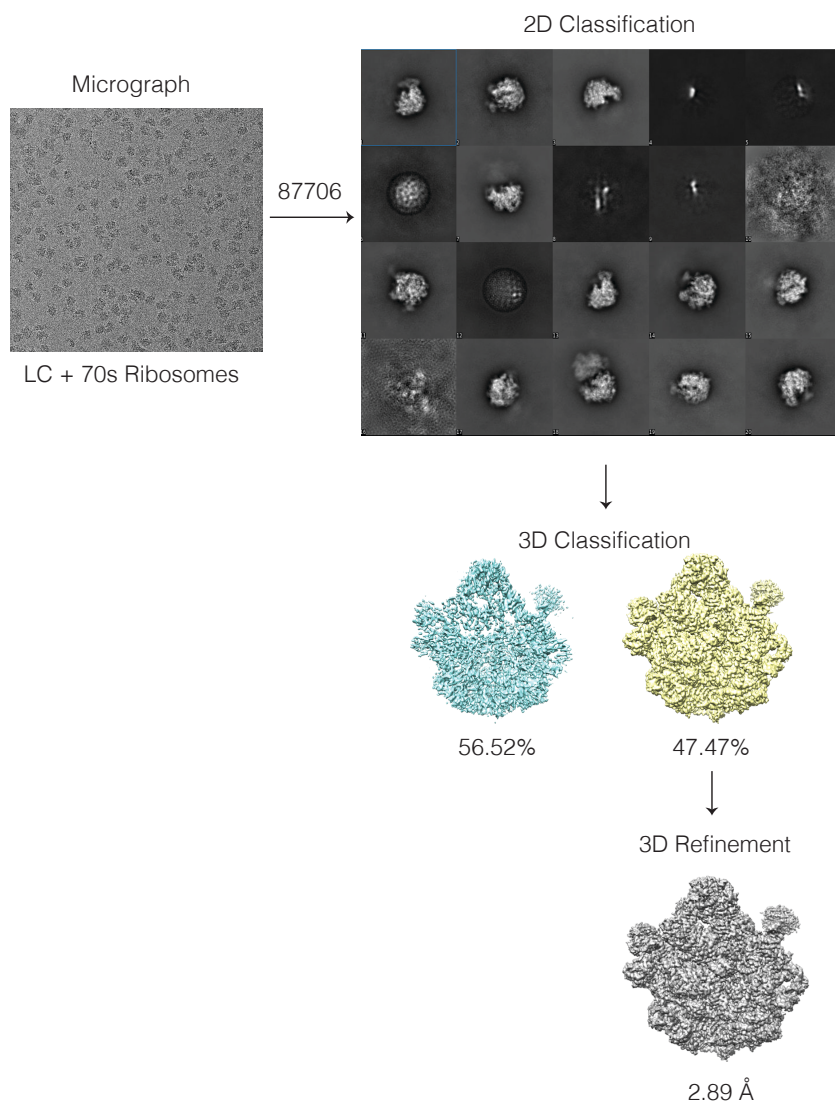


**Figure 17 |** Data collection pipeline in CisTEM for Lankacidin-C treated ribosomes. A motion-corrected micrograph, collected with a pixel size of 1.059 Å and a frame dose of 5.42 to e-/pixel/s, showcases the sample quality and particle distribution. These micrographs were then imported into CisTEM and 87706 particles were extracted and used for multiple rounds of 2D and 3D classification. After multiple rounds of manual 3D refinement, this procedure resulted in a 2.89 Å reconstruction.

## Chapter 4: Conclusions and future directions

### 4.1. Conclusions and future directions

We are only beginning to scratch the surface of how cells can read and write microtubule populations using multifaceted cellular mechanisms ranging from post-translational modifications to diverse microtubule-associated proteins. Moreover, how these layers of regulation intersect to regulate even deeper layers is an exciting challenge to pursue.

My ambitious pursuit of the αK40 loop, in order to complete the structure of tubulin, combines the structural insight of cryo-EM with the sampling efficiency of MD to investigate how PTMs can subtly transform a structural ensemble to have a major functional impact. We show that acetylation of tubulin induces electrostatic perturbations that restrict the motion of the αK40 loop, weakening lateral contacts. The sum of many weak reduced lateral contacts reduces the inter-PF interactions and may promote inter-PF sliding. The increased flexibility provided by fewer inter-PF interactions provides a mechanism by which αTAT1 can locally fine-tune the load-bearing capacity and mechanical resistance to stress of MTs. Meanwhile, deacetylation increases lateral contacts, which renders MTs inflexible, brittle, and highly susceptible to breakage under stress. The pattern of increased lateral interactions between subunits leading to mesoscale instability may be conserved in other polymeric systems[66,67]. Therefore, αK40 acetylation may function as an evolutionarily conserved "electrostatic switch" to regulate MT stability. Cancer cells may exploit this subtle form of regulation to promote cell adhesion, invasive migration, and other markers of aggressive metastatic behavior.

The further decode the tubulin code, I was excited to study the potential effects of Lankacidin group antibiotics, specifically Lankacidin-C (LC), on MTs as well as on bacterial translation because it was hypothesized to hold both antitumor and antibiotic activity! However, our MT polymerization assays and cryo-EM data show that LC exhibits strong antimicrobial activity, as previously established, but no effects on MT dynamics. Our 2.8 Å cryo-EM map improves upon the existing model and allows us to more confidently identify contacts LC makes with the PTC, whereas, our MT polymerization assays show that LC does not confer MT stability in a paclitaxel-like manner and the observed antitumor activity of LC may be due to the effects of DMSO.

In the future, it would be fascinating to probe the world of structural MAPs, or MAPs that can remodel MT macromolecular assemblies, from MT bundles to MT-motor interaction sites. These MAPs are largely intrinsically disordered and present both interesting biological questions and exciting structural questions. We may need to combine cryo-EM, cryoET, and MD to truly unravel their intricate functions and implications in disease.

## References

1.  Mitchison, T. & Kirschner, M. Dynamic instability of microtubule growth. *Nature* 312, 237–42 (1984).
2.  Howes, S. C., Alushin, G. M., Shida, T., Nachury, M. V. & Nogales, E. Effects of tubulin acetylation and tubulin acetyltransferase binding on microtubule structure. *Mol. Biol. Cell* 25, 257–266 (2014).
3.  Boggs, A. E. *et al.* α-Tubulin acetylation elevated in metastatic and basal-like breast cancer cells promotes microtentacle formation, adhesion, and invasive migration. *Cancer Res.* (2015). doi:10.1158/0008-5472.CAN-13-3563
4.  Eshun-Wilson, L. *et al.* Effects of α-tubulin acetylation on microtubule structure and stability. *Proc. Natl. Acad. Sci. U. S. A.* 116, 10366–10371 (2019).
5.  Cross, R. A. Microtubule lattice plasticity. *Current Opinion in Cell Biology* 56, (2019).
6.  Arnal, I. & Wade, R. H. How does taxol stabilize microtubules? *Curr. Biol.* (1995). doi:10.1016/S0960-9822(95)00180-1
7.  Kellogg, E. H. *et al.* Insights into the Distinct Mechanisms of Action of Taxane and Non-Taxane Microtubule Stabilizers from Cryo-EM Structures. *J. Mol. Biol.* (2017). doi:10.1016/j.jmb.2017.01.001
8.  Nogales, E., Whittaker, M., Milligan, R. A. & Downing, K. H. High-resolution model of the microtubule. *Cell* (1999). doi:10.1016/S0092-8674(00)80961-7
9.  Zhang, R., Alushin, G. M., Brown, A. & Nogales, E. Mechanistic origin of microtubule dynamic instability and its modulation by EB proteins. *Cell* (2015). doi:10.1016/j.cell.2015.07.012
10. Nogales, E., Grayer Wolf, S., Khan, I. A., Ludueña, R. F. & Downing, K. H. Structure of tubulin at 6.5 Å and location of the taxol-binding site. *Nature* (1995). doi:10.1038/375424a0
11. Fan, J., Griffiths, A. D., Lockhart, A., Cross, R. A. & Amos, L. A. Microtubule minus ends can be labelled with a phage display antibody specific to alpha-tubulin. *Journal of Molecular Biology* (1996). doi:10.1006/jmbi.1996.0322
12. Strothman, C. *et al.* Microtubule minus-end stability is dictated by the tubulin off-rate. *J. Cell Biol.* (2019). doi:10.1083/jcb.201905019
13. Mitchison, T. J. Localization of an exchangeable GTP binding site at the plus end of microtubules. *Science (80-. ).* (1993). doi:10.1126/science.8102497
14. Mitchison, T. & Kirschner, M. Dynamic instability of microtubule growth. *Nature* (1984). doi:10.1038/312237a0
15. Vainberg, I. E. *et al.* Prefoldin, a chaperone that delivers unfolded proteins to cytosolic chaperonin. *Cell* (1998). doi:10.1016/S0092-8674(00)81446-4
16. Vallin, J. & Grantham, J. The role of the molecular chaperone CCT in protein folding and mediation of cytoskeleton-associated processes: implications for cancer cell biology. *Cell Stress and Chaperones* (2019). doi:10.1007/s12192-018-0949-3
17. Lopez-Fanarraga, M., Avila, J., Guasch, A., Coll, M. & Zabala, J. C. Review: Postchaperonin tubulin folding cofactors and their role in microtubule dynamics. *Journal of Structural Biology* (2001). doi:10.1006/jsbi.2001.4386
18. Szymanski, D. Tubulin folding cofactors: Half a dozen for a dimer. *Current Biology* (2002).

doi:10.1016/S0960-9822(02)01288-5

19. Zhang, R., LaFrance, B. & Nogales, E. Separating the effects of nucleotide and EB binding on microtubule structure. *Proc. Natl. Acad. Sci. U. S. A.* (2018). doi:10.1073/pnas.1802637115

20. Tilney, L. G. *et al.* Microtubules: Evidence for 13 protofilaments. *J. Cell Biol.* (1973). doi:10.1083/jcb.59.2.267

21. Menéndez, M., Rivas, G., Díaz, J. F. & Andreu, J. M. Control of the structural stability of the tubulin dimer by one high affinity bound magnesium ion at nucleotide N-site. *J. Biol. Chem.* (1998). doi:10.1074/jbc.273.1.167

22. Nogales, E. & Zhang, R. Visualizing microtubule structural transitions and interactions with associated proteins. *Curr. Opin. Struct. Biol.* 37, 90–96 (2016).

23. Igaev, M. & Grubm, H. Microtubule instability driven by longitudinal and lateral strain propagation. *Unpublished* 1–20 (2019).

24. Walsh, G. & Jefferis, R. Post-translational modifications in the context of therapeutic proteins. *Nature Biotechnology* (2006). doi:10.1038/nbt1252

25. Magiera, M. M., Singh, P., Gadadhar, S. & Janke, C. Tubulin Posttranslational Modifications and Emerging Links to Human Disease. *Cell* (2018). doi:10.1016/j.cell.2018.05.018

26. Janke, C. & Montagnac, G. Causes and Consequences of Microtubule Acetylation. *Curr. Biol.* 27, R1287–R1292 (2017).

27. Howes, S. C., Alushin, G. M., Shida, T., Nachury, M. V. & Nogales, E. Effects of tubulin acetylation and tubulin acetyltransferase binding on microtubule structure. *Mol. Biol. Cell* (2014). doi:10.1091/mbc.E13-07-0387

28. LeDizet, M. & Piperno, G. Identification of an acetylation site of Chlamydomonas alpha-tubulin. *Proc. Natl. Acad. Sci.* (1987). doi:10.1073/pnas.84.16.5720

29. LeDizet, M. & Piperno, G. Cytoplasmic microtubules containing acetylated α-tubulin in Chlamydomonas reinhardtii: Spatial arrangement and properties. *J. Cell Biol.* (1986). doi:10.1083/jcb.103.1.13

30. De Brabander, M. J., Van de Veire, R. M. L., Aerts, F. E. M., Borgers, M. & Janssan, P. A. J. The Effects of Methyl [5-(2-Thienylcarbonyl)-1H-benzimidazol-2-yl]carbamate, (R 17934; NSC 238159), a New Synthetic Antitumoral Drug Interfering with Microtubules, on Mammalian Cells Cultured in Vitro. *Cancer Res.* (1976).

31. Dompierre, J. P. *et al.* Histone Deacetylase 6 Inhibition Compensates for the Transport Deficit in Huntington's Disease by Increasing Tubulin Acetylation. *J. Neurosci.* (2007). doi:10.1523/JNEUROSCI.0037-07.2007

32. D'Ydewalle, C. *et al.* HDAC6 inhibitors reverse axonal loss in a mouse model of mutant HSPB1-induced Charcot-Marie-Tooth disease. *Nat. Med.* (2011). doi:10.1038/nm.2396

33. Kim, J. Y. *et al.* HDAC6 Inhibitors Rescued the Defective Axonal Mitochondrial Movement in Motor Neurons Derived from the Induced Pluripotent Stem Cells of Peripheral Neuropathy Patients with HSPB1 Mutation. *Stem Cells Int.* (2016). doi:10.1155/2016/9475981

34. Li, L. *et al.* MEC-17 Deficiency Leads to Reduced -Tubulin Acetylation and Impaired Migration of Cortical Neurons. *J. Neurosci.* (2012). doi:10.1523/JNEUROSCI.0016-

12.2012

35.    Godena, V. K. *et al.* Increasing microtubule acetylation rescues axonal transport and locomotor deficits caused by LRRK2 Roc-COR domain mutations. *Nat. Commun.* (2014). doi:10.1038/ncomms6245

36.    Boggs, A. E. *et al.* alpha K40 acetylation elevated in metastatic and basal-like breast cancer cells promotes microtentacle formation, adhesion and invasive migration. 75, 203–215 (2016).

37.    Di Martile, M., Del Bufalo, D. & Trisciuoglio, D. The multifaceted role of lysine acetylation in cancer: prognostic biomarker and therapeutic target. *Oncotarget* (2015). doi:10.18632/oncotarget.10048

38.    Maruta, H., Greer, K. & Rosenbaum, J. L. The acetylation of alpha-tubulin and its relationship to the assembly and disassembly of microtubules. *J. Cell Biol.* (1986). doi:10.1083/jcb.103.2.571

39.    Portran, D., Schaedel, L., Xu, Z., Théry, M. & Nachury, M. V. Tubulin acetylation protects long-lived microtubules against mechanical ageing. *Nat. Cell Biol.* (2017). doi:10.1038/ncb3481

40.    Xu, Z. *et al.* Microtubules acquire resistance from mechanical breakage through intralumenal acetylation. *Science (80-. ).* (2017). doi:10.1126/science.aai8764

41.    Cueva, J. G., Hsin, J., Huang, K. C. & Goodman, M. B. Posttranslational acetylation of α-tubulin constrains protofilament number in native microtubules. *Curr. Biol.* (2012). doi:10.1016/j.cub.2012.05.012

42.    Chaaban, S. & Brouhard, G. J. A microtubule bestiary: structural diversity in tubulin polymers. *Mol. Biol. Cell* 28, 2924–2931 (2017).

43.    Szyk, A. *et al.* Molecular basis for age-dependent microtubule acetylation by tubulin acetyltransferase. *Cell* (2014). doi:10.1016/j.cell.2014.03.061

44.    Kull, F. J. & Sloboda, R. D. A slow dance for microtubule acetylation. *Cell* (2014). doi:10.1016/j.cell.2014.05.021

45.    Alushin, G. M. *et al.* High-Resolution microtubule structures reveal the structural transitions in αβ-tubulin upon GTP hydrolysis. *Cell* (2014). doi:10.1016/j.cell.2014.03.053

46.    Sindelar, C. V. & Downing, K. H. The beginning of kinesin's force-generating cycle visualized at 9-Å resolution. *J. Cell Biol.* (2007). doi:10.1083/jcb.200612090

47.    Egelman, E. H. The iterative helical real space reconstruction method: Surmounting the problems posed by real polymers. *J. Struct. Biol.* (2007). doi:10.1016/j.jsb.2006.05.015

48.    Lander, G. C. *et al.* Appion: An integrated, database-driven pipeline to facilitate EM image processing. *J. Struct. Biol.* (2009). doi:10.1016/j.jsb.2009.01.002

49.    He, S. & Scheres, S. H. W. Helical reconstruction in RELION. *J. Struct. Biol.* 198, (2017).

50.    Ludtke, S. J., Baldwin, P. R. & Chiu, W. EMAN: Semiautomated software for high-resolution single-particle reconstructions. *J. Struct. Biol.* (1999). doi:10.1006/jsbi.1999.4174

51.    Scheres, S. H. W. RELION: Implementation of a Bayesian approach to cryo-EM structure determination. *J. Struct. Biol.* (2012). doi:10.1016/j.jsb.2012.09.006

52.    Grigorieff, N. FREALIGN: High-resolution refinement of single particle structures. 157, 117–125 (2007).

53. Lyumkis, D., Brilot, A. F., Theobald, D. L. & Grigorieff, N. Likelihood-based classification of cryo-EM images using FREALIGN. *J. Struct. Biol.* 183, 377–388 (2013).

54. Zhang, R. & Nogales, E. A new protocol to accurately determine microtubule lattice seam location. *J. Struct. Biol.* (2015). doi:10.1016/j.jsb.2015.09.015

55. Frank, J. Time-resolved cryo-electron microscopy: Recent progress. *J. Struct. Biol.* (2017). doi:10.1016/j.jsb.2017.06.005

56. Bonomi, M., Camilloni, C., Cavalli, A. & Vendruscolo, M. Metainference: A Bayesian inference method for heterogeneous systems. *Sci. Adv.* (2016). doi:10.1126/sciadv.1501177

57. Jaynes, E. T. Information theory and statistical mechanics. *Phys. Rev.* (1957). doi:10.1103/PhysRev.106.620

58. Bonomi, M. & Vendruscolo, M. Determination of protein structural ensembles using cryo-electron microscopy. 1–22 (2018).

59. Vahidi, S. *et al.* Reversible inhibition of the ClpP protease via an N-terminal conformational switch. *Proc. Natl. Acad. Sci.* (2018). doi:10.1073/pnas.1805125115

60. Bonomi, M., Pellarin, R. & Vendruscolo, M. Simultaneous Determination of Protein Structure and Dynamics Using Cryo-Electron Microscopy. *Biophys. J.* (2018). doi:10.1016/j.bpj.2018.02.028

61. Singharoy, A. *et al.* Molecular dynamics-based refinement and validation for sub-5 Å cryo-electron microscopy maps. *Elife* (2016). doi:10.7554/eLife.16105

62. Hanot, S. *et al.* Multi-scale Bayesian modeling of cryo-electron microscopy density maps. *bioRxiv* (2017). doi:10.1101/113951

63. Yajima, H. *et al.* Conformational changes in tubulin in GMPCPP and GDP-taxol microtubules observed by cryoelectron microscopy. *J. Cell Biol.* (2012). doi:10.1083/jcb.201201161

64. Portran, D., Schaedel, L., Xu, Z., Théry, M. & Nachury, M. V. Tubulin acetylation protects long-lived microtubules against mechanical ageing. doi:10.1038/ncb3481

65. Gittes, F., Mickey, B., Nettleton, J. & Howard, J. Flexural rigidity of microtubules and actin filaments measured from thermal fluctuations in shape. *J. Cell Biol.* (1993). doi:10.1083/jcb.120.4.923

66. Eun, Y. J., Kapoor, M., Hussain, S. & Garner, E. C. Bacterial filament systems: Toward understanding their emergent behavior and cellular functions. *J. Biol. Chem.* (2015). doi:10.1074/jbc.R115.637876

67. Krupka, M. *et al.* Escherichia coli FtsA forms lipid-bound minirings that antagonize lateral interactions between FtsZ protofilaments. *Nat. Commun.* (2017). doi:10.1038/ncomms15957

68. Narayanan, A. & Jacobson, M. P. Computational studies of protein regulation by post-translational phosphorylation. *Current Opinion in Structural Biology* (2009). doi:10.1016/j.sbi.2009.02.007

69. Beltrao, P. *et al.* Evolution and functional cross-talk of protein post-translational modifications. *Mol. Syst. Biol.* (2013). doi:10.1002/msb.201304521

70. Castoldi, M. & Popov, A. V. Purification of brain tubulin through two cycles of polymerization- depolymerization in a high-molarity buffer. *Protein Expr. Purif.* (2003). doi:10.1016/S1046-5928(03)00218-3

71. Mastronarde, D. N. Automated electron microscope tomography using robust prediction of specimen movements. *J. Struct. Biol.* (2005). doi:10.1016/j.jsb.2005.07.007

72. Rohou, A. & Grigorieff, N. CTFFIND4: Fast and accurate defocus estimation from electron micrographs. *J. Struct. Biol.* (2015). doi:10.1016/j.jsb.2015.08.008

73. Emsley, P., Lohkamp, B., Scott, W. G. & Cowtan, K. Features and development of Coot. *Acta Crystallogr. Sect. D Biol. Crystallogr.* (2010). doi:10.1107/S0907444910007493

74. Hess, B., Kutzner, C., Van Der Spoel, D. & Lindahl, E. GRGMACS 4: Algorithms for highly efficient, load-balanced, and scalable molecular simulation. *J. Chem. Theory Comput.* (2008). doi:10.1021/ct700301q

75. Bonomi, M. & Camilloni, C. Integrative structural and dynamical biology with PLUMED-ISDB. *Bioinformatics* (2017). doi:10.1093/bioinformatics/btx529

76. Tribello, G. A., Bonomi, M., Branduardi, D., Camilloni, C. & Bussi, G. PLUMED 2: New feathers for an old bird. *Comput. Phys. Commun.* (2014). doi:10.1016/j.cpc.2013.09.018

77. Huang, J. & Mackerell, A. D. CHARMM36 all-atom additive protein force field: Validation based on comparison to NMR data. *J. Comput. Chem.* (2013). doi:10.1002/jcc.23354

78. Huang, J. *et al.* CHARMM36m: An improved force field for folded and intrinsically disordered proteins. *Nat. Methods* (2016). doi:10.1038/nmeth.4067

79. Michaud-Agrawal, N., Denning, E. J., Woolf, T. B. & Beckstein, O. MDAnalysis: A toolkit for the analysis of molecular dynamics simulations. *J. Comput. Chem.* (2011). doi:10.1002/jcc.21787

80. Christen, M. *et al.* The GROMOS software for biomolecular simulation: GROMOS05. *Journal of Computational Chemistry* (2005). doi:10.1002/jcc.20303

81. Tsuchiya, K., Yamazaki, T., Takeuchi, Y. & Oishi, T. Studies on T-2636 antibiotics. IV. Vitro and in vivo antibacterial activity of t-2636 antibiotics. *J. Antibiot. (Tokyo).* (1971). doi:10.7164/antibiotics.24.29

82. Ootsu, K. & Matsumoto, T. Effects of lankacidin group (T2636) antibiotics on the tumor growth and immune response against sheep erythrocytes in mice. *Gann, Japanese J. Cancer Res.* (1973). doi:10.20772/cancersci1959.64.5_481

83. Ootsu, K., Matsumoto, T., Harada, S. & Kishi, T. Antitumor and immunosuppressive activities of lankacidin group antibiotics: structure activity relationships. *CANCER CHEMOTHER.REP.* (1975).

84. Ayoub, A. T. *et al.* Antitumor Activity of Lankacidin Group Antibiotics Is Due to Microtubule Stabilization via a Paclitaxel-like Mechanism. *J. Med. Chem.* (2016). doi:10.1021/acs.jmedchem.6b01264

85. Shelanski, M. L., Gaskin, F. & Cantor, C. R. Microtubule assembly in the absence of added nucleotides. *Proc. Natl. Acad. Sci. U. S. A.* (1973). doi:10.1073/pnas.70.3.765

86. Ohi, R. & Zanic, M. Ahead of the Curve: New Insights into Microtubule Dynamics. *F1000Research* (2016). doi:10.12688/f1000research.7439.1

87. Algaier, J. & Himes, R. H. The effects of dimethyl sulfoxide on the kinetics of tubulin assembly. *Biochim. Biophys. Acta (BBA)/Protein Struct. Mol.* (1988). doi:10.1016/0167-4838(88)90078-7

88. Auerbach, T. *et al.* The structure of ribosome-lankacidin complex reveals ribosomal sites for synergistic antibiotics. *Proc. Natl. Acad. Sci.* (2010). doi:10.1073/pnas.0914100107

89. Hansen, J. L. *et al.* The structures of four macrolide antibiotics bound to the large ribosomal subunit. *Mol. Cell* (2002). doi:10.1016/S1097-2765(02)00570-1

90. Auerbach, T. *et al.* The structure of ribosome-lankacidin complex reveals ribosomal sites for synergistic antibiotics. *Proc. Natl. Acad. Sci. U. S. A.* (2010). doi:10.1073/pnas.0914100107

91. Ibba, M. & Söll, D. Aminoacyl-tRNA Synthesis. *Annu. Rev. Biochem.* (2000). doi:10.1146/annurev.biochem.69.1.617

92. Li, Q. *et al.* Synthesis and Mechanism of Action of Group a Streptogramin Antibiotics That Overcome Resistance. 5, 1–32 (2019).